

# Electrohydrodynamic Convection in Nematics

W. Pesch<sup>1</sup>, U. Behn<sup>2</sup>

<sup>1</sup> Universität Bayreuth, D-95447 Bayreuth, Germany

<sup>2</sup> Universität Leipzig, D-04109 Leipzig, Germany

**Abstract.** The purpose of this review is to present a status report on the electrohydrodynamic convection in nematic liquid crystals. The considerable progress achieved in the past two years is emphasized.

## 1 Introduction

Pattern formation in fluid systems driven away from equilibrium is a common phenomenon in nature [1, 2]. A famous canonical example is the Rayleigh-Bénard convection (RBC) in simple isotropic fluids which continues to be the subject of numerous experimental and theoretical studies (see e.g. [3]). More recently the rich variety of dynamical structures found in liquid crystals (LCs) has attracted considerable and still growing attention.

LCs are materials made up of highly anisotropic organic molecules in a state that reflects the anisotropy [4, 5]. Thus LCs have become a prime model for the study of pattern formation in anisotropic systems. There are several classes among which nematic LCs (nematics) play a dominant role in this article. Nematics are fully liquid without long-range translational, but with long-range uniaxial orientational ordering of the molecules. As a result of the coupling of the molecular alignment axis (described by the director  $\hat{\mathbf{n}}$ ) with mass flow, electric and thermal currents, the hydrodynamic equations involve numerous nonlinearities (see Sect.2), which easily lead to instabilities when a state of nonequilibrium is maintained (see e.g. [6]). Convective flows can be driven either electrically through space charges that naturally arise in an anisotropic conductor in the presence of spatial variations (electrohydrodynamic convection, EHC) or thermally through buoyancy forces (Rayleigh-Bénard convection, RBC).

EHC has attracted most of the attention and will be exclusively discussed in this review. In the typical thin-layer geometry shown in Fig.1a the nematic is sandwiched between glass plates (separation  $d \sim 10 - 100\mu$ ) with transparent electrodes. The surfaces are treated to provide uniform anchoring of the director, in most cases along the  $x$  direction ("planar" or "homogeneous" alignment), but sometimes also in the  $z$  direction ("homeotropic" alignment).

Above an applied (critical) voltage  $V_c \sim 10V$  (typically low-frequency ac) convection rolls appear with associated director distortions, which are easily detected optically. The spacing of the rolls is of order  $d$  except in the higher-frequency "dielectric range". Fig.1b shows a typical pattern with *normal* rolls, i.e. normal to the undistorted director in the  $x$  direction.

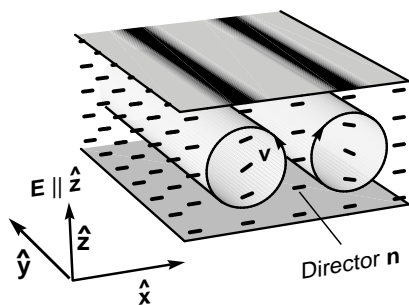


**Fig.1a.** Cell geometry with section of a roll pattern for EHC (planar configuration).  $\mathbf{E}$  = electric field,  $\mathbf{v}$  = velocity.

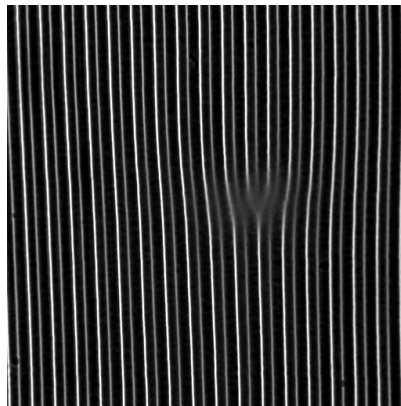


**Fig.1b.** Normal roll pattern for EHC with a dislocation.

From the experimental point of view EHC is attractive because of the easily accessible control parameters like electric and magnetic fields. The characteristic times are typically short ( $\mu$  sec) and the extension of the patterns large (up to 1000 perfectly aligned convection rolls). For the theory it is important that spatio-temporal complexity appears quite often already in the vicinity of the convection onset. Thus common perturbational schemes, like the order parameter approach can be put on a sound basis and their reliability can easily be evaluated.

Liquid crystals are complicated and an intuitive understanding of all the mechanisms hidden in the nematohydrodynamic equations is not easy. In fact, the remarkable progress in the last two decades is not imaginable without the particularly close collaboration between experimental and theoretical groups in this field. There are numerous examples (only some of which we will mention explicitly) where experimental findings have motivated the theoretical efforts and vice versa. For a classical review of convective instabilities in LCs, see [7] and for EHC one may consult the books of Blinov [8] and Pikin [9] and the review articles [10, 11, 12, 13, 14]. In recent overviews [15, 16] in particular

the progress achieved in the years from 1984 - 1996 was emphasized.

The investigation of convection scenarios in LCs is also a problem of materials. In experiments the standard reference materials MBBA (4-methoxybenzylidene-4'-n-butyl-aniline) or a mixture, Merck Phase 5, have typically been used (sometimes doped with an ionic substance). These are the only room-temperature nematics with dielectric anisotropy,  $\epsilon_a < 0$ , where virtually all the material parameters have been measured (for tabulated values: see e.g. [17] for MBBA, [18] for Phase 5 and references therein). Since these nematics are similar in their properties, the investigation of other classes is highly desirable and promising. A recent successful example is the new very stable material I52 (4-ethyl-2-fluoro-4'-[2-(trans-4-n-pentylcyclohexyl)-ethyl]-biphenyl) doped with iodine [19, 20]. Even at onset qualitatively new localized structures ("worms") [21] have been detected, which provide a new challenge for the theory. This applies also to materials where one can switch continuously from the nematic to the smectic phase by decreasing the temperature [22].

In the present article we will concentrate on the most recent results in various realizations of EHC. In addition we will focus on an interesting topic in detail which could be addressed only briefly in the previous reviews [15, 16] because of space limitations. The restoring forces on the director in LCs are not very strong and its dynamics is susceptible to very weak external bias. In hindsight it is therefore not too surprising that for the first time the influence of thermal noise on a continuous nonequilibrium phase transition was successfully analyzed in nematics [23, 24]. In this paper it will be demonstrated that a *controlled* application of noise is very attractive both from the experimental and theoretical point of view.

After the introduction and explanation of the basic equations (Sect.2) the theoretical concepts (the linear and weakly nonlinear analysis) will be sketched in Section 3. Section 4 deals with various new aspects of EHC in the planar configuration and in Section 5 the homeotropic configuration is discussed. Section 6 is devoted to the noise-driven EHC near threshold. Finally, in the General Conclusions (Sect. 7), we shall mention some perspectives for future work. Furthermore a brief connection to other hydrodynamic instabilities in nematics is made.

## 2 Basic equations and instability mechanisms

The dynamics of liquid crystals is described by a well accepted set of macroscopic equations (see e.g. [4, 5, 25, 26]). Here we will sketch only the most simplest version pertaining to nematic LCs.

In the nematic state the isotropy is spontaneously broken and the averaged molecular orientation is described by the director  $\mathbf{n}$ , i.e. a unit vector where  $\pm\mathbf{n}$  are equivalent. The dynamical **balance of torques** on the director  $\mathbf{n}$  is determined by:

$$\gamma_1 \mathbf{n} \times \dot{\mathbf{n}} = \mathbf{n} \times (\mathbf{h}_{el} + \mathbf{h}_{vis}) \quad (1)$$

where the dot stands for the material derivative  $\frac{d}{dt} + \mathbf{v} \cdot \nabla$ . In Eq. (1), the elastic molecular field,  $\mathbf{h}_{el}$ , derives from the elastic free energy density  $f_{el}$ :

$$f_{el} = \frac{1}{2} [k_{11}(\nabla \cdot \mathbf{n})^2 + k_{22}(\mathbf{n} \cdot \nabla \times \mathbf{n})^2 + k_{33}(\mathbf{n} \times \nabla \times \mathbf{n})^2] - \frac{1}{2} \mu_0 \chi_a (\mathbf{n} \cdot \mathbf{H})^2 - \frac{1}{2} \epsilon_0 \epsilon_a (\mathbf{n} \cdot \mathbf{E})^2 \quad (2)$$

according to the relationship

$$(\mathbf{h}_{el})_i = -\frac{\partial f_{el}}{\partial n_i} + \partial_j \frac{\partial f_{el}}{\partial (\partial_j n_i)}. \quad (3)$$

The  $k_{11}, k_{22}, k_{33}$  terms are associated with splay, twist and bend distortions of the director field. The importance of electric ( $\mathbf{E}$ ) and magnetic ( $\mathbf{H}$ ) contributions is determined by the anisotropy of the magnetic and electric susceptibilities  $\chi_a = \chi_{\parallel} - \chi_{\perp}$  and  $\epsilon_a = \epsilon_{\parallel} - \epsilon_{\perp}$ , respectively.

The viscous part of the molecular field,  $\mathbf{h}_v$ , can be written as:

$$\mathbf{h}_v = -\alpha_2 \mathcal{D} \cdot \mathbf{n} - \alpha_3 \mathbf{n} \cdot \mathcal{D} \quad (4)$$

where the tensor  $\mathcal{D}$  characterizes the velocity shear ( $\mathcal{D}_{ij} = \partial v_i / \partial x_j$ ). Since  $\alpha_2 < 0$ , and  $\gamma_1 = \alpha_2 - \alpha_3 > 0$  (see Eq.(1) with  $|\alpha_2| \gg \alpha_3$ ) the torque tends to rotate the director in order to avoid the director-transverse velocity gradients  $\mathbf{n} \times \mathcal{D}\mathbf{n}$ .

The **momentum balance** results in the (generalized) Navier-Stokes equation for the velocity field

$$\rho_m \frac{d\mathbf{v}}{dt} = \mathbf{f}_B + \nabla \cdot \mathbf{T} \quad (5)$$

with the bulk force  $\mathbf{f}_B$  to be discussed below and the stress tensor

$$T_{ij} = -p\delta_{ij} - \frac{\partial f_{el}}{\partial n_{k,i}} n_{k,j} + t_{ij} \quad (6)$$

where  $\rho_m$  denotes the mass density and  $p$  the pressure. The viscous contribution  $t_{ij}$  contains the six Leslie shear viscosity coefficients  $\alpha_i$  [27]

$$t_{ij} = \alpha_1 n_k n_m A_{km} n_i n_j + \alpha_2 n_i N_j + \alpha_3 n_j N_i + \alpha_4 A_{ij} + \alpha_5 n_i n_k A_{kj} + \alpha_6 n_j n_k A_{ki}. \quad (7)$$

with the positional strain tensor  $A_{i,j} = 1/2(\mathcal{D}_{i,j} + \mathcal{D}_{j,i})$ . There exists also an orientational strain ( $\sim \alpha_2, \alpha_3$ , cf Eq.(7)) which is associated with the director dynamics relative to the local solid body rotation (with the rate  $\frac{1}{2}\text{curl}\mathbf{v}$ ):

$$\mathbf{N} = \frac{d\mathbf{n}}{dt} - \frac{1}{2}(\text{curl}\mathbf{v} \times \mathbf{n}). \quad (8)$$

With the use of an Onsager relation  $\alpha_6 - \alpha_5 = \alpha_2 + \alpha_3$  the number of independent parameters can be reduced [28]. Incompressible flow is assumed

( $\nabla \cdot \mathbf{v} = 0$ ), which is guaranteed by the introduction of the toroidal and poloidal velocity potentials (see [29]).

Crucial for the occurrence of EHC is the bulk force  $\mathbf{f}_B$  in the Navier-Stokes equation (5):

$$\mathbf{f}_B = \rho_{el}\mathbf{E} + (\mathbf{P} \cdot \nabla)\mathbf{E}, \quad \mathbf{P} = (\epsilon - 1)\mathbf{E}. \quad (9)$$

The first term in  $\mathbf{f}_B$  is the classical Coulomb force on the charge density  $\rho_{el}$ . Much less important is ponderomotive force in the second term which contains the macroscopic polarization  $\mathbf{P}$  (for the dielectric tensor  $\epsilon$  see Eq.(11)). In principle there exist also flexoelectric contributions to  $\mathbf{P}$  [30, 31]. They seem to be negligible except for very thin cells and for not too large ac frequencies [32, 16, 26]. The equation determining  $\rho_{el}$  is obtained from charge conservation and Poisson's law

$$\frac{d\rho_{el}}{dt} + \nabla \cdot (\boldsymbol{\sigma} \cdot \mathbf{E}) = 0, \quad \rho_{el} = \nabla \cdot (\boldsymbol{\epsilon} \cdot \mathbf{E}). \quad (10)$$

Here the dielectric and conductivity tensors  $\boldsymbol{\epsilon}$  and  $\boldsymbol{\sigma}$  (typical for uniaxial anisotropy) are given by:

$$\epsilon_{i,j} = \epsilon_{\perp} + \epsilon_a n_i n_j; \quad \sigma_{i,j} = \sigma_{\perp} + \sigma_a n_i n_j. \quad (11)$$

The assumption of an anisotropic, but fixed ohmic conductivity is characteristic for the standard model. A more general ansatz (the "weak-electrolyte" model, WEM [33]) is discussed in Section 4.2.

According to the standard model (SM) described above one can distinguish between three relaxation-time scales for the director ( $\tau_d$ ), the velocity ( $\tau_{visc}$ ) and the charge ( $\tau_q$ ). The following expressions are easily derived:

$$\tau_d = \gamma_1 d^2 / (\pi^2 k_{11}), \quad \tau_{visc} = 2\rho_m d^2 / (\pi^2 \alpha_4), \quad \tau_q = \epsilon_0 \epsilon_{\perp} / \sigma_{\perp}. \quad (12)$$

$\tau_d$  is typically the longest time (1 – 10 sec) followed by  $\tau_q$  ( $\sim 10^{-3}$  s). Even shorter is  $\tau_{visc}$  ( $10^{-5}$  s). Thus the velocity field can usually be treated adiabatically (neglect of "inertial terms").

Now we are in a position to discuss the basic driving mechanism for EHC. The important point is that in almost all nematics  $\sigma_a$  is substantially positive (typically  $\sigma_a / \sigma_{\perp} \sim 0.3 - 1$ ). Choosing materials with negative or only slightly positive dielectric anisotropy  $\epsilon_a$  (here the materials show great diversity) one easily sees that in the presence of an applied field  $\mathbf{E}$  and with a (small) spatial fluctuation of the director  $\mathbf{n}$  a space charge  $\rho_{el}$  results (no solution of Eqs. (10) with  $\rho_{el} = 0$ ). Roughly speaking the charges are focused at locations where the director bends. The bulk force in the Navier-Stokes equation (5) may then overcome viscous stresses and drive a velocity field  $\mathbf{v}$ . Via the viscous coupling (see Eq.(1)) this may enhance the spatial variation of the director and thus generate an instability. For low frequencies and for materials with not too large dielectric anisotropy the threshold voltage is of the order  $V_c \approx \sqrt{\pi^2 k_{11} / (\sigma_{\perp} \tau_q)}$  and the introduction of the reduced control parameter  $R = V^2 \frac{\sigma_{\perp} \tau_q}{\pi^2 k_{11}}$  is often useful.

### 3 Elements of the Theoretical Analysis

The theoretical methods for analyzing pattern forming instabilities are quite extensively discussed in the literature (see e.g. [2, 34, 35] and [36] in particular for nematics) The set of macroscopic equations as presented in the previous section can be written in the following symbolic form:

$$\mathcal{L}\mathbf{V} + \mathbf{N}_2(\mathbf{V}|\mathbf{V}) + \mathbf{N}_3(\mathbf{V}|\mathbf{V}|\mathbf{V}) + \dots = (\mathcal{B}_0 + \mathcal{B}_1(\mathbf{V}) + \mathcal{B}_2(\mathbf{V}|\mathbf{V}))\frac{\partial\mathbf{V}}{\partial t}. \quad (13)$$

$\mathbf{V} = (\phi, \mathbf{n}, \mathbf{v}, \dots)$  stands for the collection of field variables involved in EHC; they are chosen in such a way that  $\mathbf{V} = 0$  corresponds to the nonconecting ("basic", "primary") state. The components of the vector operators  $\mathbf{N}_2, \mathbf{N}_3 \dots$  are quadratic, cubic... in  $\mathbf{V}$  and its spatial derivatives, whereas the quantities  $\mathcal{L}$  and  $\mathcal{B}_i$  represent matrix differential operators of the order in  $\mathbf{V}$  indicated. A reformulation of Eq.(13) in Fourier space is often appropriate with respect to the horizontal directions  $\mathbf{x} = (x, y)$  of "infinite" extent. In the transverse direction ( $z$ ) the boundary conditions are satisfied by expanding  $\mathbf{V}$  with respect to a suitable complete set of test functions (Galerkin method).

The onset of the instability is obtained from a standard linear stability analysis of the basic (primary) state. For a certain Fourier mode  $\mathbf{U}(\mathbf{q})$  with the wave vector  $\mathbf{q} = (q, p)$  one arrives from Eq. (13) at an eigenvalue problem:

$$\lambda\mathcal{B}_0(i\mathbf{q}, \partial_z, R)\mathbf{U}_{\mathbf{q}}(z) = \mathcal{L}(i\mathbf{q}, \partial_z, R)\mathbf{U}_{\mathbf{q}}(z), \quad (14)$$

where  $R$  denotes the main control parameter (e.g. the squared voltage in the case of EHC).

The eigenvalue  $\lambda(\mathbf{q}, R) = \sigma(\mathbf{q}, R) \pm i\Omega(\mathbf{q}, R)$  with the largest real part, determines the growthrate  $\sigma$  and the frequency  $\Omega$  of planforms near onset. The condition  $\sigma(\mathbf{q}, R) = 0$  defines the neutral surface  $R = R_0(\mathbf{q})$ . Minimizing  $R_0(\mathbf{q})$  with respect to  $\mathbf{q}$  gives the threshold  $R_c = R_0(\mathbf{q}_c)$  with the critical wavevector  $\mathbf{q}_c = (q_c, p_c)$  and the critical frequency  $\Omega_c = \Omega(\mathbf{q}_c)$ , which vanishes for a stationary bifurcation (the more common case) but differs from zero for a Hopf (oscillatory) bifurcation.

In an axially anisotropic system like planar EHC, one speaks of "normal" rolls (see Fig.1a) if  $\mathbf{q}_c$  is parallel to the preferred direction ( $p_c = 0$ ). If  $\mathbf{q}_c$  is at an oblique angle, one speaks of "oblique" rolls (see Fig.2a below). Clearly one then has the two symmetry-degenerate directions ("zig" and "zag") which may superpose to give rectangles. In the case of a Hopf bifurcation one has a degeneracy between waves traveling in opposite directions, which may also superpose to give standing waves. In the oblique-roll case even four degenerate modes are involved.

In EHC, for the usual case of driving with a pure ac field of angular frequency  $\omega = 2\pi f$ , the eigenvector  $\mathbf{U}_{\mathbf{q}}$  of Eq.(14) inherits the additional periodic time dependence and the eigenvalue  $\lambda$  becomes a Floquet coefficient. Then there is an additional discrete symmetry  $(z, t) \rightarrow (-z, t + 1/(2f))$  and

each component of  $\mathbf{U}_{\mathbf{q}}$  has a definite parity: Generally the "conductive" mode (nonvanishing time average of all fields except the induced electric potential  $\phi$ ) destabilizes first at low frequencies  $f$ . Above a "crossover frequency"  $f_d$  the "dielectric" mode with the opposite parity determines the threshold. The existence of these two regimes planar EHC was first pointed out by the Orsay group [37, 38] (for further details see [12, 13, 16]).

A good understanding of the regime slightly above threshold is conventionally achieved by the weakly nonlinear analysis [39, 40, 1, 34]. The basic idea in its rather general form (for a recent more detailed presentation see [41, 42, 36]), is to reduce the phase-space dimension of the system by expanding  $\mathbf{V}$  in an appropriate basis of states, characterized as the "dynamically active" ones [34]. At first the linear modes in Eq. (14) of positive or slightly negative growthrate are included in this set. Their expansion coefficients  $A(\mathbf{q})$  correspond to order parameters, which vanishes at threshold. By a systematic expansion up to cubic order in  $A$  one arrives at the order parameter equations for the  $A(\mathbf{q})$  [36, 43, 41], which permit the calculation of roll solutions and their stability at threshold. In particular the universal features become more transparent when the order parameter equations are reformulated in real space in terms of amplitude (envelope) or Ginzburg-Landau equations (GLE), for which the fast spatial variations ( $\sim q_c^{-1}$ ) are separated out. This real-space formulation is essential when it comes to the description of more complex spatio-temporal patterns with disorder and defects, which have been studied extensively in EHC slightly above threshold (see Fig.1b). One ends up with the famous (slightly generalized) Ginzburg Landau equation [44]

$$\partial_t A = \lambda(\mathbf{q}_c - i\nabla, \epsilon)A - \gamma|A|^2 A \quad (15)$$

where  $\lambda$  is the linear growth rate of Eq.(14). Clearly  $\lambda$  is zero at threshold  $\epsilon = (R - R_c)/R_c = 0$ ,  $\nabla = 0$  and should be expanded in both arguments. At threshold it is sufficient to keep the following terms

$$\lambda(\mathbf{q}_c - i\nabla, \epsilon) \approx \epsilon + \xi_1^2 \partial_x^2 + 2a\xi_1 \xi_2 \partial_x \partial_y + \xi_2^2 W \partial_y^2 - iZ\xi_1 \xi_2^2 \partial_x \partial_y^2 - \xi_2^4 \partial_y^4. \quad (16)$$

The various constants in Eq.(16) determine the curvature of the neutral curve at  $\epsilon = 0$ .

On this level the expansion can be cast into an overall expansion scheme in terms of  $\epsilon^{1/2}$ , or equivalently  $A$ . In the anisotropic case, where there is no continuous degeneracy of the critical mode(s), one may in general assume  $\epsilon \sim A^2 \sim \partial_t \sim \partial_x^2 \sim \partial_y^2$ , so that the higher order terms  $\sim \partial_x \partial_y^2$  and  $\partial_y^4$  drop out ( $W = O(1)$ ). The terms in Eq. (15) thus become uniformly of order  $\epsilon^{3/2}$ .

Going back to Eqs.(15, 16) with  $a = 0$  it is easy to see that a decrease of  $W$  from positive to negative value owing to the change of some secondary control parameter, like the frequency in EHC describes a transition from normal to oblique rolls. Details of this transition, which is the analog of a Lifshitz point in the theory of equilibrium phase transitions, have been

discussed elsewhere [45, 17, 46, 47]. The corresponding uniform scaling  $\sim \epsilon^{3/2}$  as in Eq.(15) is recovered with  $W \sim \epsilon^{1/2} \sim \partial_x$  and now  $\partial_y \sim \epsilon^{1/4}$ . This corresponds to the scaling adopted in isotropic media. In fact the well-known Newell-Whitehead-Segel amplitude equation for isotropic systems [48, 49] can now be obtained as the special case  $W = 0$  and  $Z = \pm 2$  in Eq.(16). In the case of a Hopf bifurcation (as observed in EHC) all the coefficients of Eq.(15,16) become complex. The resulting celebrated "complex Ginzburg-Landau equation" (CGLE) exhibits transitions (e.g. at the Benjamin-Feir instability) to various forms of spatio-temporal chaos and is presently studied intensely (for general reviews see e.g. [2, 34]).

The general structure of GLE's can be deduced a priori from the symmetries in a system as for instance the invariance properties with respect to space- and time translations or suitable reflections. The symmetries also manifest themselves in the linear growth-rate function (16). In simple cases very few coefficients determine the GLE, which can be extracted by comparison with the experiments. But in general for a quantitative comparison with experiments the often tedious calculation of the coefficients is inevitable [17, 12, 41, 50, 33, 16].

The GLE(15) determines only the stability of rolls with respect to disturbances of the generalized Eckhaus type, i.e. slow modulations of the roll spacing and undulations along the roll axis [45]. For the description of secondary bifurcations and modulated roll patterns away from threshold the weakly nonlinear analysis must be extended through the consideration of additional modes. For instance nonanalytic "mean flow" contributions of the order  $\sim A^2$  have been included [43, 51].

In the simplest version the equation for the mean-flow amplitude  $B$  assumes the form:

$$(c_1 \partial_x^2 + c_2 \partial_y^2) B = q_1 \partial_x \partial_y |A|^2 + q_4 \partial_y (i A^* \partial_y^2 A + c.c.) + \dots \quad (17)$$

Eq.(15) is supplemented by a coupling term  $\sim A \partial_y B$ . The mean flow is excited by long-wavelength modulations of the pattern  $A(x, y, t)$ . Since the field  $B$  satisfies an anisotropic Poisson equation, its long-range character is evident. In nematics the mean flow turns out to enhance transverse modulations ( $q_4 > 0$ ) in distinct contrast to isotropic fluids in most cases ( $q_4 < 0$ ) [43].

Very recently it has been emphasized that in EHC other slowly damped modes have to be included in the set of active modes besides mean flow. Their inclusion leads to additional equations, which have a structure similar to Eq.(17). Most important are the twist modes of the director  $\mathbf{n}$ , which correspond to a rotation of  $\mathbf{n}$  in the plane of the layer. They are weakly damped and can easily be excited near threshold. In the case of homeotropic alignment with rotational invariance this is obvious [52]. Any configuration with a finite in-plane component of the director spontaneously breaks a continuous symmetry, namely the isotropy. The growthrate of the associated Goldstone

modes, which tend to restore the isotropy by a rotation of the in-plane director approaches zero in the homogenous case and is consequently small for slow modulations. But in the planar case inspite of the elastic torques due to anchoring of the director at the boundaries the damping of the twistmode is also weak [56].

The coupling of a short-wavelength patterning mode to a weakly damped long-wavelength one (like a Goldstone mode) readily leads to complex-spatio-temporal patterns at threshold. One should mention a 1d model for seismic waves, where a spontaneous symmetry breaking is also important [53] or the coupling to a concentration mode in binary fluids [54]. The occurrence of localized "worm" structures [21] and their modelling by a slow "charge-mode" [55] will be discussed in Sect.4.2.

An order-parameter approach for the regime further above threshold is certainly less systematic than the derivation of Eq.(15) since for instance the  $\epsilon$ -scaling is no longer beneficial. Therefore fully nonlinear calculations are indispensable. One follows the approved method in isotropic RBC: Galerkin expansions are applied and the resulting coupled highly nonlinear equations for the expansion coefficients are solved by Newton methods. Afterwards the solutions are tested for stability.

On the basis of numerical results and of comparison with experiments it has been demonstrated that EHC in nematics is one of the very few cases where secondary (and even higher bifurcations) can be captured semi-quantitatively by an order-parameter approach (see e.g. [56]). A further very useful simplified description makes use of a suitable phase-diffusion equation ([57]), which allows for a transparent description of the quite intricate bifurcation scenarios in EHC [58]. Convection instabilities in nematics are therefore an important paradigm for the validation of a reduced dynamical description of pattern forming systems in general.

## 4 EHC in the planar configuration

### 4.1 General background

The mechanism for the instability in EHC is based mainly on space charges generated by preferential conduction along  $\hat{\mathbf{n}}$  ("charge focusing", see Sect.2). The basic idea has been suggested by Carr [59] and incorporated into a first one-dimensional model by Helfrich [60]. A first generalization to include the common case of  $ac$  driving followed almost immediately [37, 38]. It became clear that one has to distinguish between the low-frequency "conductive" and the "dielectric" regime above a certain transition frequency  $f_d$ . In the following sections we will first concentrate on the conductive regime.

For example, the need to go beyond one dimensional models became evident on the basis of the observation of specific three-dimensional structures, called **oblique** rolls [61, 62, 63, 64]. At low frequencies they can nucleate already at threshold, but otherwise appear at a secondary bifurcation. A

representative pattern is shown in Fig.2a. One observes domains with two symmetry-degenerate directions ("zig" and "zag") separated by walls. Note that such a kind of spontaneously broken chiral symmetry is unique for anisotropic systems. In fact, the fully three dimensional linear stability analysis of the standard nematohydrodynamic equations (see Sect.2 and ,e.g., [17, 16] for references) has yielded the properties at onset of the instability: the threshold voltage and the wavevector of the twodimensional patterns. The agreement between experimental and theoretical results is typically quite satisfactory (see Fig.2b).

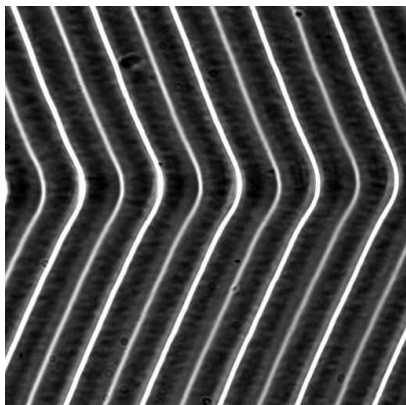


**Fig.2a.** Zig-zag pattern after increasing the voltage in Fig.1b.

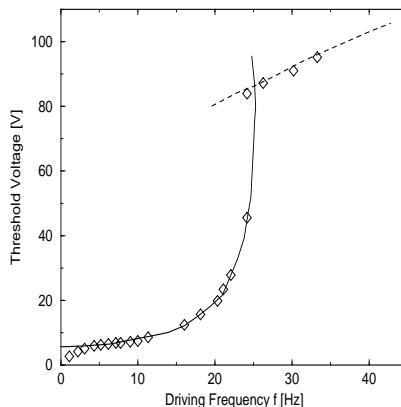


**Fig.2b.** Threshold curve for EHC as function of frequency. Experimental points from [65].

However the "standard model", SM, as described in Sect.2, where LCs are treated as ohmic conductors is incapable of explaining the Hopf bifurcation leading to travelling waves, which are often observed in sufficiently thin layers (below about  $50\mu$ ) and clean materials (low conductivity) [63, 66, 67, 68]. An extension (the "weak-electrolyte model", WEM), where electric transport in the nematic is described in terms of two mobile ion species (of opposite charge) which are coupled via a slow dissociation-recombination reaction [69, 33] has proven to be successful (see Sect.4.2).

In the further progress of the theory the weakly nonlinear analysis in terms of Ginzburg-Landau amplitude equations [17, 12] have provided information on the Eckhaus stability boundaries of periodic roll patterns, in good agreement with experiments [70, 71, 72]. An even more sensitive test is the analysis of the dynamics and interaction of defects (dislocations) in ideal patterns, which compares well with experiments [73, 74, 75, 76] too. It was realized that mean-flow effects are very important in the transition

from ordered periodic to weakly turbulent patterns [47, 77, 78, 43] (for a phenomenological treatment, see [79, 80, 81, 82]).

Fully nonlinear theoretical studies have followed [83], which put the concept of **abnormal** rolls, at first observed in homeotropic EHC, [84] on a sound basis. At low frequency their bifurcation is usually preceded by a long-wavelength zig-zag instability; at higher frequency they appear after a secondary bifurcation of normal rolls. The wave vector of abnormal rolls is parallel to the preferred  $x$ -direction, but the underlying director field has experienced a spontaneous rotation in the  $x-y$  plane. Previous experimental findings in EHC in different geometries are now understood for the first time and new experimental activities have been motivated. The abnormal rolls will be discussed in detail in Sect.4.3. Very recently the dielectric regime has attracted considerable attention. For instance a first convincing explanation for the common chevron pattern has been given (see Sect.4.4).

#### 4.2 The weak electrolyte model (WEM)

The WEM model [33, 69] has provided the basis for the understanding of the Hopf bifurcation observed quite frequently at threshold [85, 86]. For a Hopf bifurcation two processes that compete on a comparable time scale are necessary. One might think of the director and charge relaxations, but they do not compete. Instead they support each other usually; in addition the time scales (12) are very different; the director relaxation is much slower than all other processes, and thus determines the dynamics.

According to the WEM model it is assumed that a slow process is connected with the relaxation of the mobile ion densities  $n^+$  and  $n^\perp$  on the time scale  $\tau_{rec}$ , which may result from a dissociation-recombination reaction. One thus obtains for singly charged ions

$$\rho_{el} = e(n^+ - n^\perp), \quad \sigma = \sigma \sigma', \quad (18)$$

where

$$\sigma = e(\mu_\perp^+ n^+ + \mu_\perp^\perp n^\perp), \quad \sigma'_{ij} = \delta_{ij} + \frac{\sigma_a}{\sigma_\perp} n_i n_j. \quad (19)$$

Here  $\mu_\perp^\pm$ ,  $\mu_\parallel^\pm$  are the ionic mobilities perpendicular and parallel to the director, respectively. For simplicity the anisotropies have been assumed to be the same for both types of ions so that  $\sigma_a/\sigma_\perp = \mu_\parallel^\pm/\mu_\perp^\pm - 1$ . Thus  $\sigma$  is an additional variable now. From the balance equations for  $n^+$  and  $n^\perp$  one easily recovers Eq.(10) and in addition one obtains

$$\begin{aligned} & \frac{d\sigma}{dt} + \nabla \cdot [((\mu_\perp^+ + \mu_\perp^\perp)\sigma + \mu_\perp^+ \mu_\perp^\perp \rho_{el})] \\ &= \frac{\sigma_{eq}}{2\tau_{rec}} \left[ 1 - \frac{(\sigma + \mu_\perp^+ \rho_{el})(\sigma_\perp \mu_\perp^+ \rho_{el})}{\sigma_{eq}^2} \right] \approx \frac{1}{\tau_{rec}} \left[ (\sigma - \sigma_{eq}) + \frac{\mu_\perp^+ \mu_\perp^\perp}{2} \rho_{el} \right], \end{aligned} \quad (20)$$

where  $\sigma_{eq} = e(\mu_\perp^+ + \mu_\perp^\perp)n_{eq}$  contains the equilibrium ion density  $n_{eq}$ . The last expression is obtained by linearization in the quantities  $n^+ - n_{eq}$  and

$n^\perp - n_{eq}$ . In this model the effect of ion accumulation on the conductivity is thus included, whereas ionic diffusion is neglected as in the SM. The charge accumulation counteracts the standard (Helfrich) mechanism of generation of space charges. If the time scale  $\tau_{rec}$  is sufficiently slow one can expect to find an oscillatory behavior of the system at threshold, i.e. a Hopf bifurcation.

The detailed linear stability calculations for the WEM model have been performed [69, 33] using the same approximations that led to the analytic threshold formulas within the SM [87, 17, 12, 16]. It is found that there is an upward shift in the stationary threshold, which may be quite small, and more importantly, that indeed a Hopf bifurcation occurs [85, 18] with critical frequency

$$\omega_H \tau_d = 2\pi f_H \tau_d = \frac{R_c \tilde{\alpha} C}{1 + \omega'^2} \sqrt{1 - \left( \frac{(1 + \omega'^2) \lambda_\sigma \tau_d}{R_c \tilde{\alpha} C} \right)^2}, \quad (21)$$

when the expression under the square root is positive. Here  $R = V^2 \frac{\sigma_\perp \tau_q}{\pi^2 k_{11}}$  is the reduced control parameter (see Sect.2),  $\tilde{\alpha}^2 = \mu_\perp^+ \mu_\perp^- \gamma_1 \pi^2 / (\sigma_\perp d^2)$  is proportional to the geometric means of the mobilities and  $\omega' = \omega \tau_q \beta$  with  $\beta = \frac{(\sigma_{||}/\sigma_\perp)q'^2 + p'^2 + 1}{(\epsilon_{||}/\epsilon_\perp)q'^2 + p'^2 + 1}$  is a reduced frequency. Moreover  $\lambda_\sigma = -[\tau_{rec}^{-1} + \bar{\tau}_d^{-1} R \tilde{\alpha}^2 \beta / (1 + \omega'^2)]$  ( $< 0$ ) is the damping rate of the (new) WEM mode. Its dominant contribution is usually just determined by the ion recombination rate  $1/\tau_{rec}$ . The factor  $C$  [33] contains only SM quantities and is about one (see Ref. (28) in [86] for a misprint in [33]).

For the Hopf bifurcation to occur, i.e. for a positive argument of the square root in Eq.(21), the quantity  $\tau_d / (\tilde{\alpha} \tau_{rec})$  must be sufficiently small. This requires that the recombination of ions is sufficiently slow and that the layer is sufficiently thin and clean. Note, however, that for materials with negative dielectric conductivity, where  $R_c$  diverges at the cutoff frequency  $f_d$  (in the approximation used), the Hopf condition is always satisfied near the cutoff, and the Hopf frequency, which is then just given by the prefactor of the square root in Eq.(21), becomes large there. This appears to be consistent with the experiments [63, 66, 67]. Moreover, the prediction of the theory, that for materials with vanishing dielectric anisotropy the Hopf frequency becomes essentially independent of the external frequency, has been verified experimentally using the material I52 [85]. I52 has the property that  $\epsilon_a$  changes from negative to positive values when the temperature is increased through  $T \approx 60^\circ\text{C}$ .

A quantitative test of Eq.(21) with experiments has been performed recently for the nematic Phase 5, where (almost) all material parameters have been measured. In Fig.3a the Hopf frequency (21) is shown as function of the ac frequency (solid line). The units are chosen according to the predicted theoretical scaling behavior:  $\omega_h \sim d^{\perp 3} \sigma_\perp^{\perp 1/2}$  is easily obtained from Eq. (21), if the  $d$ -dependencies of the director relaxation time  $\tau_d$ , the threshold  $R_c$

and of  $\tilde{\alpha}$  are combined; the proportionality  $\sim \sigma_{\perp}^{1/2}$  is due to  $\tilde{\alpha}$ . The ac-frequency scale in  $\omega'$  is set by  $\tau_q$ . The agreement with the WEM theory is very convincing.

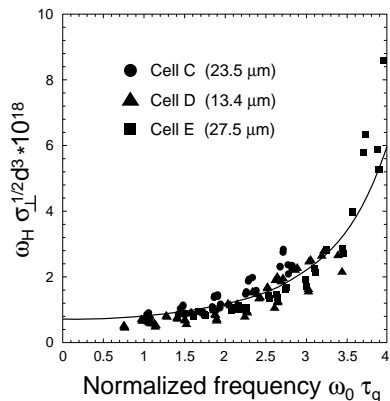


**Fig.3a.** The Hopf frequency of traveling rolls multiplied by  $(\sigma_{\perp}^{eq})^{1/2} d^3$  (see text).

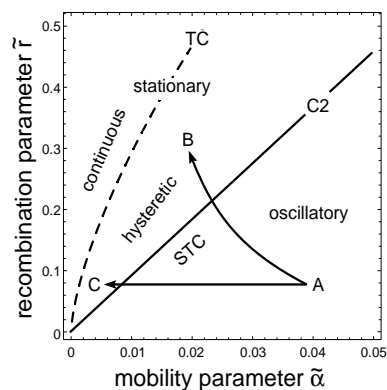


**Fig.3b.** Phase diagram in the  $\alpha - r$  plane (see text)

Subsequently a weakly nonlinear analysis of the WEM model has been performed [86] in order to determine the bifurcation type at threshold. Some results are shown Fig. 3b. In dependence on the mobility parameter  $\tilde{\alpha}$  and the recombination parameter  $\tilde{r} = \tau_d / \tau_{rec}$  one finds below the curve labelled  $C2$  a supercritical Hopf bifurcation. In the regime bounded by  $C2$  and the curve labelled  $TC$  the bifurcation is stationary and hysteretic, while above  $TC$  one finds a continuous stationary bifurcation. In the limit  $\tilde{r} \rightarrow \infty$  the standard model is recovered. The point  $A$  corresponds to the experiments discussed in [21] for the material I52 at  $30^{\circ}C$ . The arrow to point  $C$  indicates a change of the bifurcation type as the temperature is increased to  $60^{\circ}$ . In contrast to the SM the bifurcation scenarios depend also on the cell thickness  $d$ : The arrow to  $B$  corresponds to a doubling of  $d$ .

As has already been mentioned, the WEM model has first been compared with experiments for the new nematic I52 [85]. Recently two-dimensional localized states, called 'worms' (see the snapshots in Fig.4), have been described in this material [88, 21]. They are localized and have a unique, small width in the  $y$  direction but are of much a greater varying length along  $\hat{x}$ , i.e. the anisotropy axis. Rapidly traveling waves in one direction  $\parallel \hat{x}$  pass under a slowly moving envelope moving in the opposite direction. Their number increases with increasing voltage and they tend to grow by coalescing until at higher voltage the cell is filled with convection.

The theoretical analysis of the worms is challenging. One-dimensional pulses have been experimentally discovered in binary fluids [89, 90] and have been obtained as solutions of the one-dimensional CGL [91] (for further references, see [55]). Two-dimensional localization in such hydrodynamic pattern-forming systems is not well documented in experiments. From theoretical studies (see e.g. [92, 93]) one expects that 2d-localized structures can be obtained in the case of a subcritical Hopf bifurcations. Thus an ad hoc model [94] has been proposed in the form of an anisotropic Swift-Hohenberg equation with adjustable complex coefficients and a quintic nonlinearity to capture the subcritical bifurcation. It is not too surprising that indeed localized structures similar to the experiments could be produced. However, the basic assumption of the subcritical Hopf bifurcation in planar EHC is in conflict with theory and experiments [95].

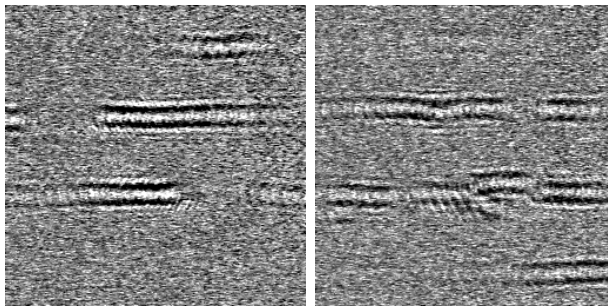


**Fig.4.** Localized worm structures for  $\epsilon = 0.012$  (left) and for  $\epsilon = 0.057$  (right) (Courtesy G. Ahlers)

Therefore a more realistic model was recently proposed [55] where two amplitude equations for oblique travelling rolls were coupled to a slow mode, which might be identified with the charge-accumulation mode. Even details of the experiments could be reproduced satisfactorily. From a theoretical point of view the model is also very interesting, since it involves a new mechanism for the localized states. One has a forward Hopf bifurcation for extended cell-filling patterns in agreement with the “microscopic” theory [86]. However, the transition to localized states is predicted to be hysteretic in line with the recent experimental results [95]. The final step, i.e. the derivation of the new equations from the WEM model, has not yet been accomplished.

While the localized worms are certainly spectacular in EHC for I52, the cell filling-states developing from the supercritical Hopf bifurcation are also very interesting. The system is below a Lifshitz point, obviously with a bifurcation of four degenerate oblique-roll solutions (zig-zag, left-right traveling).

Their interaction can easily lead to various types of spatio-temporal chaos (STC) near threshold [96], which can be controlled through a variation of the conductivity of the nematic. The experimental have stimulated efforts of theoretical modeling [97].

### 4.3 Abnormal rolls

Conventional normal rolls (NR) can only exhibit point defects (dislocations). Oblique rolls (OR) break the reflection symmetry  $y \rightarrow -y$  and thus can show in addition line defects (grain boundaries) separating domains with wavevectors  $(q, p)$  (“zig”) and  $(q, -p)$  (“zag”) [98, 99]. In Fig.5a,b typical grain boundaries along  $\hat{x}$  and  $\hat{y}$  are shown for the nematic Phase 5.

Surprisingly, in an apparently NR structure, line defects have been observed as well. With increasing voltage (i.e.  $\epsilon$ ) the angle between the roll axis and  $\hat{y}$  is found to systematically decrease and may even reach zero. In this process the grain boundary of Fig.5b is transformed into the wall of Fig.5c. That the two domains on either side of the wall are not equivalent becomes more evident as  $\epsilon$  is further increased. Indeed, one then observes the branching of an additional wavevector  $(k_x, +k_y)$  on the right side, and  $(k_x, -k_y)$  on the left side (see Fig.5d).

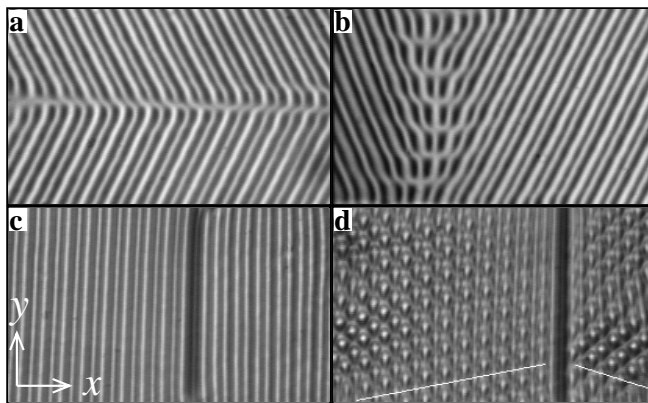


**Fig.5.** Representative snapshots of the experimental evolution of electroconvection in a cell of thickness  $5\mu\text{m}$ , at  $\omega\tau_0 = 0.3$ . a, b: zig-zag structures near threshold ( $\epsilon \sim 0.02$ ), with “horizontal” and “vertical” grain boundaries. c: wall at  $\epsilon \sim 0.40$  originating from the grain boundary of b. d: varicose structures at  $\epsilon \sim 0.70$ , originating from the structure c. The two modulation directions are indicated by the white lines.

The existence of a two-variant state of normal rolls indicates a new sym-

metry breaking. Those rolls have been named “*abnormal rolls*” (AR), a term introduced in the context of homeotropically aligned cells [84] for rolls with an optically detected symmetry breaking, see Sect.5 below.

AR cannot be understood by the standard weakly nonlinear approach where the roll structure is characterized unambiguously by its wavevector and the linear eigenvector at threshold (see Sect.3).

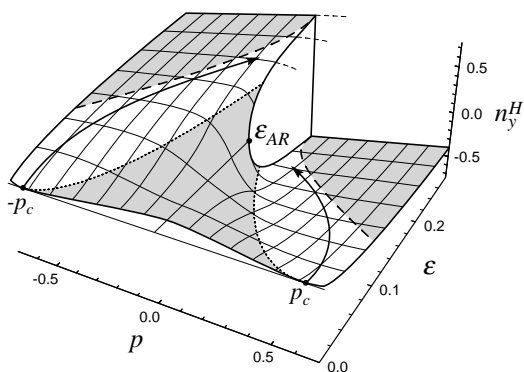


**Fig.6** Amplitude  $n_y^H$  of the twist mode in roll patterns of wavevector  $\mathbf{q} = (q, p)$ , as a function of  $p$  and  $\epsilon$  at  $\omega\tau_0 = 0.3$  (parameters of Phase 5). Unstable regions in gray (Eckhaus boundary dotted, Bimodal Varicose boundary dashed). Arrows: sketch of the experimental evolution of  $p(\epsilon)$ . In the experiments also  $q$  evolves with  $\epsilon$ , which leads to quantitative changes of the diagram.

The key result of a fully nonlinear Galerkin analysis is presented in Fig.6. It shows the amplitude  $n_y^H$  of a twist mode corresponding to a *homogeneous rotation* (i.e. independent of  $x, y$ ) of the director in the  $x, y$  plane as function of  $\epsilon$  and  $p$  for roll solutions with  $\mathbf{q} = (q, p)$ . This rotation is symmetric with respect to the mid plane of the layer, and is largest there. At  $p = 0$ ,  $n_y^H$  vanishes if  $\epsilon$  is sufficiently small, in agreement with the predictions of the weakly nonlinear theory. The novel and striking feature is the pitchfork bifurcation at a secondary transition point  $\epsilon = \epsilon_{AR}$  to a state with  $n_y^H \neq 0$  (at  $p = 0$  !). In these AR the  $y \mapsto -y$  symmetry is spontaneously broken without tilting of the rolls. In addition the amplitude of the (periodic)  $n_z$  component, which increases like  $n_z \sim \sqrt{\epsilon}$  for small  $\epsilon$ , as expected from the weakly nonlinear theory, is found to remain nearly constant for  $\epsilon \geq \epsilon_{AR}$ . For  $p \neq 0$  the director “prefers” to rotate towards the axis of the rolls: e.g.  $n_y^H < 0$  for  $p > 0$  (see the lower sheet in Fig.6).

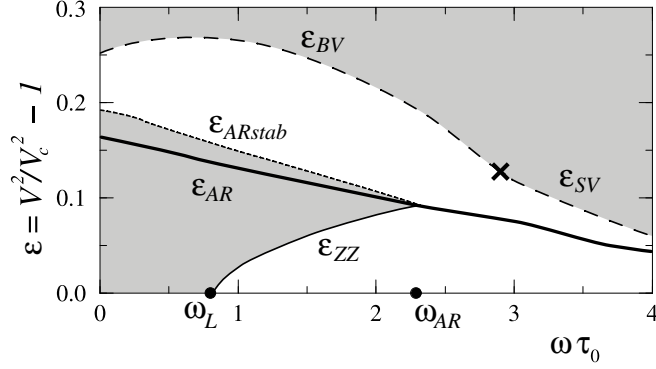


Fig.7. Stability diagram for rolls in the normal direction ( $p = 0$ ) in the  $\omega, \epsilon$  plane (unstable regimes in gray).  $\epsilon_{AR}$  (thick line): NR  $\rightarrow$  AR bifurcation.  $\omega_L =$  Lifshitz frequency,  $\epsilon_{ZZ}$  (thin line): zig-zag instability,  $\epsilon_{ARstab}$  (dotted line): restabilization of the abnormal rolls. The upper dashed line is at low frequencies a short-wavelength varicose instability ( $\epsilon_{BV}$ ) that transforms into a long-wavelength skewed-varicose instability ( $\epsilon_{SV}$ ) at  $\omega\tau_0 \simeq 2.8$  (x).

In Fig.7 the stability regime (in white) for rolls with  $\mathbf{q} = (q_c, 0)$  is shown in more detail in the  $\epsilon, \omega$  plane. For  $\omega < \omega_L$ , where the primary bifurcation is to OR, NR are unstable near threshold ( $\epsilon \simeq 0$ ) against long-wavelength undulations along the roll axis (“zig-zag” instability). The mechanism becomes less efficient for AR, where the  $y \mapsto -y$  symmetry is broken. Thus AR become stable when  $|n_y^H|$  is large enough, for  $\epsilon > \epsilon_{ARstab}(\omega)$  (dotted line). When  $\epsilon$  is increased further the AR are destabilized at  $\epsilon_{BV}(\omega)$  (dashed line), now by a short-wavelength instability with a new wavevector  $|\mathbf{k}| \simeq q_c$  roughly parallel to the homogeneous part of the in-plane director  $(n_x^H, n_y^H)$  in the AR. The bimodal patterns in Fig.5d then obviously result from the destabilisation of AR at  $\epsilon = \epsilon_{BV}$  (see Fig.7).

In an intermediate frequency range  $\omega_L < \omega < \omega_{AR}$ , NR are stable for  $\epsilon \leq \epsilon_{ZZ}(\omega)$  (solid line). At  $\epsilon_{ZZ}$  a zig-zag instability (ZZ) develops [100], which derives continuously from the oblique rolls at onset for low  $\omega$ :  $\epsilon_{ZZ}(\omega) \rightarrow 0$  for  $\omega \rightarrow \omega_L$ . Above  $\epsilon_{ZZ}$  the situation is analogous to the low-frequency regime, i.e. one gets stable AR for  $\epsilon > \epsilon_{ARstab}$ . When  $\epsilon$  is increased further the AR experience the varicose destabilisation at  $\epsilon_{BV}$  as before.

The stability limits  $\epsilon_{AR}, \epsilon_{ARstab}$  and  $\epsilon_{BV}$  decrease with increasing  $\omega$  as seen in Fig.7. Above the frequency  $\omega_{AR}$ , where  $\epsilon_{ZZ}, \epsilon_{ARstab}$  meet the line  $\epsilon_{AR}$ , the bifurcation NR  $\rightarrow$  AR occurs *in the stable range*. Along the varicose line  $\epsilon_{BV}(\omega)$ , the modulation wavevector  $\mathbf{s} = \mathbf{k} - \mathbf{q}$  approaches zero with increasing  $\omega$ , whereas the ratio  $s_y/s_x$  stays finite ( $s_y/s_x \simeq \pm 2.7$ ). Above

$\omega\tau_0 \simeq 2.8$  (see the cross in Fig.7), the varicose instability thus becomes a long-wavelength modulational instability of the skewed-varicose type [101]. The substance MBBA has no Lifshitz point. Therefore the part of the stability diagram for  $\omega > \omega_L$  in Fig.7 is shifted to lower  $\omega$ .

The detailed bifurcation sequences can be discussed with the help of Fig.8 at a representative frequency  $\omega\tau_0 = 0.5$  for patterns with wave vectors  $\mathbf{q} = (q_c, p)$ . In contrast to Fig.6 the amplitude  $n_y^H$  is not shown. For  $\epsilon \leq \epsilon_{zz} \sim 0.05$  normal rolls ( $p = 0$ ) are stable. Above  $\epsilon_{zz}$  a bifurcation to oblique rolls with finite  $p$  takes place, where a whole  $p$  band is available except for the unstable "bubble" marked by the dashed line. At  $\epsilon_{ARstab}$  (in the  $ZZ$ -unstable regime within the bubble) abnormal rolls bifurcate. They become  $ZZ$ -stable at  $\epsilon_{ARstab}$ .

It seems that in experiments when slowly increasing  $\epsilon$  beyond  $\epsilon_{ZZ}$  the patterns follow at first more or less the boundary curve of the unstable bubble. Thus the angle  $\alpha = \arctan(q/p)$  of the wavevector with respect to the  $x$ -axis does not become too large. The pattern appearing beyond the  $ZZ$ -instability can be described at first as rolls with a smooth undulation along their axis. If  $\epsilon$  is increased further (presumably above  $\epsilon_{AR}$ ) zig-zag patterns with sharp boundaries as shown in Fig.2a develop. The sequence NR-undulated rolls-OR has been first described in Ref. [62]. For higher  $\epsilon \leq \epsilon_{BV}$  it is a pattern selection problem whether the system actually uses the opportunity to return to AR patterns with  $p = 0$  or not. In most experiments reported up to now  $p$  decreases but  $p = 0$  is not reached (except in the case of a wall as in Fig.5c). However, there is a new very promising approach to map the stability diagram in Figs. 7,8. directly. A strip-like cell is used where straight rolls along the long side seem to be strongly preferred such that above  $\epsilon_{AR}$  perfect AR are recovered. The whole scenario is quite complicated and involves modulated roll patterns, which can exist in the unstable bubble when decreasing  $\epsilon$  starting from above  $\epsilon_{ARstab}$ . There exist already first results based on a phase diffusion equation which seem to explain the rather intricate phenomena [58, 57].

In Ref. [83] further examples are given which prove that the concept of abnormal rolls is very important for EHC in nematics. There exists semi-quantitative agreement with experiments, which now allow for a new interpretation. This applies for instance to various kinds of (dynamic) defect structures [98, 99, 102], which are presumably triggered by the SV-instabilities in Fig.7. The bifurcation phenomena in particular associated with abnormal rolls appear to be generic for planar nematic convection, since they are also found in Rayleigh-Bénard convection of nematics [56].

Finally one might ask why abnormal rolls have escaped the attention of experimentalists until quite recently. The direct observation of a homogeneous  $n_y$  distortion in the planar configuration is difficult. The optical axis of the uniaxial nematics is the director. Maximal optical contrast is achieved in extraordinary light, when the polarization of the light is parallel to the

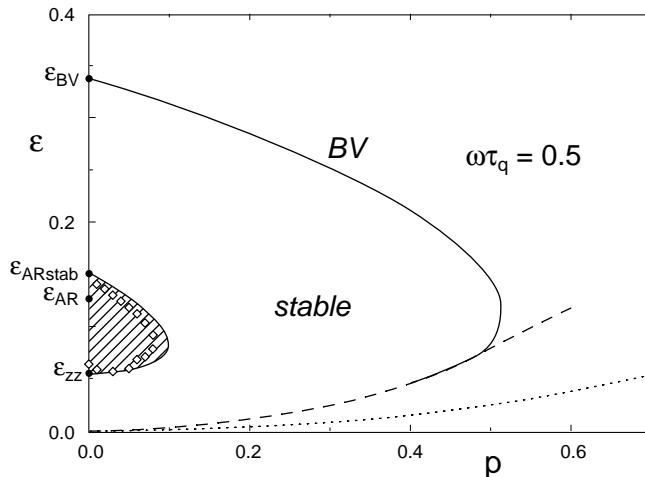


**Fig.8.** Stability diagram (MBBA) for rolls escaping in the oblique direction at fixed ( $q = q_c$ ) The unstable bubble was tested with Galerkin expansions truncated at four (shaded) and six terms (diamond)

director at the plates,  $\hat{\mathbf{x}}$ . The polarization then follows adiabatically any  $n_y$  excursion in the bulk and exits parallel to  $\hat{\mathbf{x}}$  again, as long as  $n_y$  varies slowly over a wavelength of the light (Mauguin's principle). Therefore only  $n_z$  is monitored, whereas the  $n_y$  distortion has almost no effect on the propagation of the rays. An exception is the grain boundary in Fig.5c with opposite  $n_y^H$  orientations on either side. The resulting strong  $n_y$  gradients inside the grain, coupled to a localized peak of  $n_z$ , explain the observed optical contrast of the wall. However, a small modification of the optical setup permits to visualize the small differences between clockwise and counterclockwise twisted domains in general. The trick is to lift the (optical) equivalence according to Mauguin's principle through the introduction of a quarter-wave plate at a  $45^\circ$  orientation to  $\hat{\mathbf{x}}$  [103]. It is also very illuminating to observe the slow relaxation time of the twist mode. At first a strong in-plane rotation is seeded in an abnormal roll pattern for  $\epsilon \geq \epsilon_{AR}$ . Then  $\epsilon$  is suddenly quenched to zero. While the pattern itself vanishes almost immediately, it takes much longer time for the director to turn back in the  $x$  direction.

#### 4.4 Dielectric regime

In the dielectric regime (see Sect.3) the director and the velocities oscillate with the external frequency about the basic state while the polarity of the

space charge remains time independent in leading order. The theoretical analysis of the patterns follows in principle the techniques already approved in the conduction regime.

With respect to the linear regime it is not difficult to determine numerically the critical wavevector and the onset voltage. The salient features are however already contained in an approximate analytic threshold formula, which can be derived with the help of appropriate lowest-order test functions [16, 104]. In comparison with the conductive regime convection sets in at a higher voltage, which increases continuously with the ac-frequency  $\omega$ . In order to overcome the stabilizing dielectric torque larger in-plane gradients are required for the convection destabilisation and thus the wavelength increases a function of  $\omega$ . Unless the critical wavelength becomes comparable to the cell thickness the dielectric instability is a "bulk instability" which is insensitive to the boundary conditions. The wavelength is determined by the diffusion length of the bend deformation  $k_{33}/(\gamma_1\omega)$ , i.e. by material parameters and not by the vertical distance  $d$  of the cell boundaries. The convection rolls are very thin and the pattern looks like a planar lamellar structure. Consequently the appropriate order parameter in the dielectric regime is the d-independent electric field instead of the voltage as in the conductive regime.

In addition one finds from the analytical formulation that the threshold stays finite for  $\epsilon_a \rightarrow 0$ , and in fact remains so when  $\epsilon_a$  becomes positive. This appears to be in conflict with early treatments [38], but improved formulas have been developed later [105, 7]. Very recent and particularly careful measurements of the linear properties in the nematic Phase 5 agree very well with the theory [106]. In MBBA the measured threshold exceeds typically the theoretical prediction. The reason might be, that MBBA is a quite unstable nematic and thus its conductivity increases with time due to molecular dissociation processes. In addition dopants are often added to increase the conductive frequency range. It has never been tested systematically whether the commonly used material parameter may not have to be modified accordingly. Also the flexoelectric effects could be more important than in the conduction regime [104]. On the other hand it is reassuring that quite subtle properties like the phase shift of the director oscillations with respect to the applied voltage compare favourably with experiment [107].

Passing to the weakly-nonlinear dielectric regime the lamellar-type structure is only weakly anchored at the boundaries and it should be easily destabilized by (slow) transverse modulations. Thus it is not surprising that again the twist mode is found to be responsible for a secondary bifurcation to abnormal rolls, typically at a very small  $\epsilon \sim 10^{-2}$  [104]. The results are consistent with recent experiments in Phase 5, where the dielectric regimes takes over at a small frequency ( $f_d = 26 Hz$ ) [108]. The secondary instability is found at a rather small  $\epsilon_{sb} \leq 0.08$ . As already stated abnormal rolls at a very small  $\epsilon$  were also found directly in an particularly designed experimental setup [103].

With increasing  $\epsilon$  the situation becomes simpler at least from the experimental point of view. We again refer to the recent experiment [108]; above  $\epsilon_{sb}$  the rolls become slightly undulated and a persistent dynamics is introduced by the appearance of well separated dislocations. The number of these dislocations increases continuously and above  $\epsilon = 0.24$  one observes periodically ordered chains of dislocations oriented along the normal-roll direction. The polarity of the defects is the same along each chain and alternates from chain to chain. The defects move in alternating directions (for a snapshot see Fig.9). The name "chevron structure" has been coined for this pattern, which is known for many years (see e.g [109]).

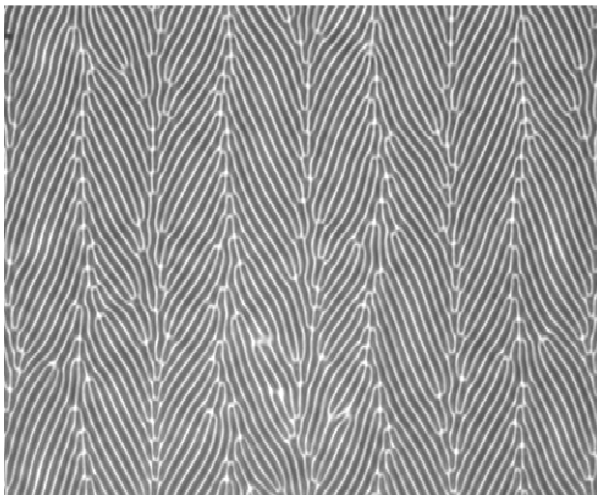


**Fig.9.** Chevron pattern at  $\epsilon = 0.26$  in Phase 5 [108]

Recently a first theoretical explanation has been proposed for the chevrons [110]. The starting point are Eqs.(24, 25) (see Section 5) originally derived for homeotropic EHC. They describe the coupling of the patterning mode  $A$  to the order parameter of the abnormal rolls (i.e. the in-plane director  $\mathbf{c}$  with an angle  $\phi$  relative to the  $x$  axis). In the dielectric as well as in the homeotropic case the convection starts in a situation where the electric field is perpendicular to the in-plane director  $\mathbf{c}$ , which is subject to a very weak external torque. The boundary effects in the dielectric case can be identified with the action of a small magnetic field  $\mathbf{H}$  parallel to  $\mathbf{x}$  in the homeotropic case. In some parameter regimes defect-chaotic solutions (see Figs.12, 13) are indeed observed in simulations of Eqs.(24, 25), when  $h^2 = H^2/(-2\Gamma\epsilon)$

drops below a critical value  $O(1)$  (corresponding to small anchoring). With increasing  $\epsilon$  the defects become then ordered in chevron-like stripes as in Fig. 9 [111].

The quite regular chevrons at larger  $\epsilon$  can then be captured theoretically by a coarse-grained description in terms of reaction-diffusion equations [111, 110]. The key to the formation of chevrons is the “anomalous” torque on  $\mathbf{c}$ , which already leads to the abnormal-roll bifurcation at small  $\epsilon$  and to defect chaos with increasing  $\epsilon$ . When the density of defects is sufficiently high a topological charge field can be defined as the difference between the densities of defects with positive and negative polarity. The chaotic motion of the defects leads to a finite diffusivity of the topological charge density. In the theoretical description the angle  $\phi$  plays the role of an activator, which enhances the (local) topological charge imbalance. The reason is that the rolls tend to follow the rotation of  $\mathbf{c}$ . The resulting reorientation of the roll pattern entails the motion of defects with oppositely charges in opposite directions, which then play the roll of an inhibitor. Elastic effects are responsible for diffusion in  $\phi$ . Once having arrived at the level of a reaction-diffusion systems the possible scenarios are well known: One can have either oscillatory instabilities or a steady spatially periodic Turing pattern, which, in the present system, is identified with the chevron structure.

## 5 EHC in the homeotropic configuration

In this chapter we will discuss in some detail the electrohydrodynamic instabilities in the homeotropic configuration. The general setup is very similar to Fig.1a except that the director is initially oriented parallel to the electric ac field  $\mathbf{E} \parallel \mathbf{z}$  by an appropriate surface treatment of the confining plates. The system is now isotropic in the plane of the nematic layer. We will address the case of negative dielectric anisotropy  $\epsilon_a < 0$ , where, for energetic reasons, the director has the tendency to orient perpendicular to  $\mathbf{E}$  in order to minimize the electric torque. For the case of positive  $\epsilon_a$ , see e.g. [112, 113, 16]. If  $\mathbf{E}$  (or the applied voltage  $V = |\mathbf{E}|d$ ) is strong enough to overcome the opposing elastic torque at first the homogeneous Freédericksz transition [4, 5] shows up, which is a equilibrium transition. The isotropy is then spontaneously broken and a definite orientation of the in-plane director component is singled out, which we call the  $x$ - axis. In some cases an additional magnetic field  $\mathbf{H} \parallel \mathbf{x}$  is applied perpendicular to  $\mathbf{E}$  to lift the rotational invariance and to single out a definite orientation. Under the combined action of  $H$  and  $V$  the Freédericksz transition takes place if

$$\left(\frac{V}{V_F}\right)^2 + \left(\frac{H}{H_F}\right)^2 \geq 1. \quad (22)$$

is fulfilled [4].  $V_F$  and  $H_F$  are defined as:

$$V_F = \pi \sqrt{\frac{k_{33}}{|\epsilon_a| \epsilon_0}}, \quad H_F = \frac{\pi}{d} \sqrt{\frac{k_{33}}{|\chi_a| \mu_0^{\perp 1}}} \quad (23)$$

where  $\epsilon_a$  and  $\chi_a$  are the dielectric and diamagnetic anisotropies, respectively, and  $k_{33}$  is the elastic bend constant (see Sect.2). By testing experimentally the transition lines according to the inequality (22) one can check for imperfections in the anchoring of the director at the cell boundaries [106].

Above the Fréedericksz transition a planar layer develops in the central region of the cell. In view of the obvious analogy to the planar configuration it is not too surprising that it can become unstable against a convection instability above a second threshold. The transitions are sketched in Fig.10.

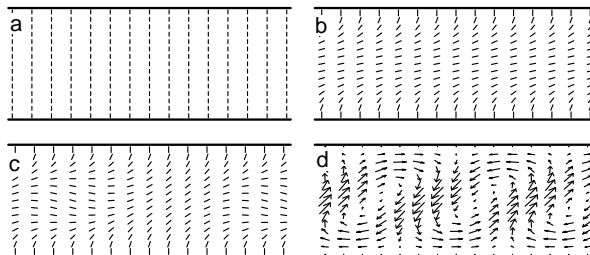


**Fig.10** a) Homeotropic groundstate, b) Director configuration after the Fréedericksz transition c) Modulated director configuration in the EHC state. d) Velocity field in the EHC state.

The theoretical analysis of the bifurcations is more complicated than in the planar configuration due to the inhomogeneous ground state. It has been achieved with the use of Galerkin-expansions [112] which are numerically demanding. The linear analysis reproduces the scenarios already known from planar EHC. At low frequencies oblique rolls, at higher frequencies, above a Lifshitz point  $\omega_L$ , normal rolls are found. By further increasing the frequency one switches at  $\omega = \omega_f$  from the conductive to the dielectric regime. The agreement with experiments is very satisfactory [106].

In Fig.11a the secondary destabilisation of normal rolls at  $\omega\tau_0 = 1$  is shown as function of an imposed planar magnetic field  $H$  on the basis of a full Galerkin calculation (GAL). For a sufficiently strong magnetic field a

long wavelength zig-zag instability is obtained. The details become clearer from Fig.11b, where the secondary destabilisation  $\epsilon_{sb}$  is shown as function of  $\omega\tau_0$  for a fixed magnetic field ( $H = 1$ ). Starting from the Lifshitz point (near  $\omega\tau_0 = 0.6$ ) the zig-zag line increases continuously. Near  $\omega\tau_0 = 1.5$  there is an abrupt change to the homogeneous abnormal-roll bifurcation. The bifurcation scenario is in perfect analogy to the planar case (see Figs.7,8). The bifurcation lines do not join smoothly at the Lifshitz point. This is explained by the fact that the stability of patterns with the critical wavevector  $\mathbf{q}_c = (q_c, p_c)$  is shown. Approaching  $\omega_L$  from above the bifurcation point  $\epsilon_{ZZ}$  (the lowest point of the bubble in Fig.8), moves down until it vanishes at  $\omega_L$ . Below  $\omega_L$  the bubble is deformed and increasingly less important for increasing  $p$ ; the patterns remain stable up to much higher  $\epsilon$ .

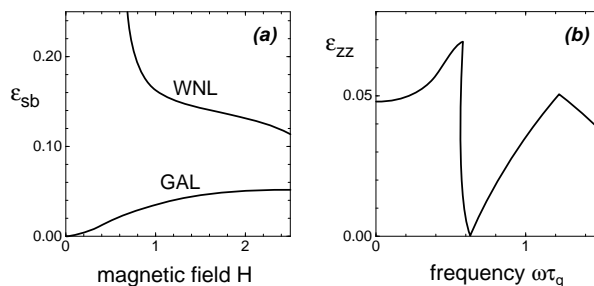


**Fig.11** a) Secondary destabilisation  $\epsilon_{sb}$  of normal rolls at bandcenter for  $\omega\tau_0 = 1.0$  (GAL: Full Galerkin analysis; WNL: weakly nonlinear analysis. b) Secondary destabilisation of normal rolls at bandcenter as function of the frequency  $\omega\tau_q$  for the reduced magnetic field  $h_x = 1$ , from [112].

However, in the limit of zero magnetic field, when the preferred axis, i.e. the in-plane director  $\hat{\mathbf{c}}$ , is not fixed externally, the analogy to the planar case breaks down. This is already evident from Fig.11a where normal rolls become unstable immediately at threshold. The reason is that transverse modulations lead to a torque on  $\hat{\mathbf{c}}$  which cannot be compensated. Oblique roll solutions do not even exist because of this torque [114]. Even with a finite magnetic field the standard weakly nonlinear analysis breaks down (see the curve WNL in Fig.11a) because the rotation of  $\hat{\mathbf{c}}$  becomes too large.

The important difference between the homeotropic and the planar case has been explained in Sect.3 in terms of the Goldstone mode associated with the spontaneously broken isotropy due to the Fréedericksz transition. The action of the Goldstone mode corresponds to a rotation of the director in the plane, i.e. to a finite  $n_y$  component, with a nonvanishing  $z$ -average. There is

in fact a close analogy to the AR bifurcation and the abnormal rolls have been identified at first in the homeotropic case [84].

The absence of stable roll patterns has led to the conjecture of a new type of spatio-temporal chaos at onset [114]. A convincing experimental confirmation is shown in Fig.12. On the right side the oblique-roll pattern for a frequency below the Lifshitz point (upper panel) and normal rolls (lower panel) for the frequency above the Lifshitz point are stabilized by a magnetic field. Switching off the magnetic field leads within seconds to the disordered patterns shown on the left hand side.

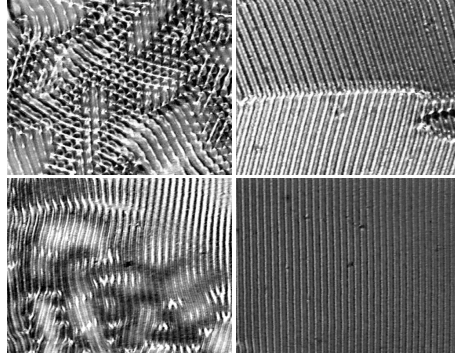


**Fig.12** Experimental pictures from [115]. Typical convection patterns with (left panel) and without magnetic field (right panel) are shown at two different frequencies, 60 Hz (above) and 300 Hz (below)

A clear understanding of the disordered patterns near threshold has been achieved from a novel weakly nonlinear description that incorporates the critical convection mode together with the Goldstone mode [52].

The general form of the equations is governed by symmetry considerations (we write  $\hat{\mathbf{c}}_{\perp} = \hat{\mathbf{z}} \times \hat{\mathbf{c}}$ ):

$$\begin{aligned} \tau \partial_t \tilde{A} = & \left[ \varepsilon + \xi_{xx}^2 (\hat{\mathbf{c}} \cdot \partial_{\mathbf{r}} - iq_c)^2 + \xi_{yy}^2 (\hat{\mathbf{c}}_{\perp} \cdot \partial_{\mathbf{r}})^2 \right. \\ & \left. - g |\tilde{A}|^2 + i \beta_y \hat{\mathbf{c}}_{\perp} \cdot \nabla \varphi \right] \tilde{A}, \end{aligned} \quad (24)$$

$$\begin{aligned} \gamma_1 \partial_t \varphi = & K_3 \hat{\mathbf{c}}_{\perp} \cdot \nabla^2 \hat{\mathbf{c}} + (K_1 - K_3) \hat{\mathbf{c}}_{\perp} \cdot \nabla (\nabla \cdot \hat{\mathbf{c}}) \\ & + \chi_a (\hat{\mathbf{c}} \cdot \mathbf{H}) (\hat{\mathbf{c}}_{\perp} \cdot \mathbf{H}) + \frac{\Gamma}{4} (-iq_c \tilde{A}^* (\hat{\mathbf{c}}_{\perp} \cdot \partial_{\mathbf{r}}) \tilde{A} + \text{c.c.}). \end{aligned} \quad (25)$$

The various coefficients in Eqs.(24,25) can be obtained from the Galerkin code used for Fig.11.

At first one recognizes a generalized Swift-Hohenberg equation for the pattern amplitude  $A$  in Eq.(24) where the local coordinate system is determined by the (local) anisotropy axis  $\hat{\mathbf{c}} = (\mathbf{cos}(\phi), \mathbf{sin}(\phi))$ . The torque due to spatial modulations exerted on the in-plane director is included in Eq. (25). where in addition the magnetic torque is taken into account.

These equations have been used for numerical simulations. In Fig.13 a representative snapshots of  $\psi = \tilde{A} + c.c.$  (left side) is compared with experimental observations (right side) for  $\varepsilon = 0.02, H = 0$  [116]). Material parameters as in [114] have been used to calculate the coefficients of (24,25) (for details see [52]). Evidently the patterns in experiments and simulations look very similar. Though in the normal roll regime some defects appear, the rolls are locally aligned along a main direction. The oblique roll regime is dominated by a superposition of zig and zag. Again the preferred axis changes only over large distances. A persistent time dependence is observed in the simulations in agreement with the experiments in the oblique roll case. However, the experiments in the normal roll regime at higher frequency reveal two different regimes near threshold [106, 117, 118]. First a frozen-in disordered pattern is observed which looks like the one shown in Fig.13 (lower left panel). When the control parameter is increased a crossover to a time dependent disordered patterns is found. It is not yet clear whether an important term is missing in Eqs. (24,25), or whether small inhomogeneities in the experimental cell suppress a persistent dynamics at threshold.

Equations (24,25) represent normal-form equations for quasi-2D pattern-forming systems with a novel kind of symmetry, and thus should be of general interest. Other realizations might be found in convection instabilities in smectic-C liquid crystals, where a  $\hat{\mathbf{c}}$ -director exists ab initio, and in Rayleigh-Bénard convection of homeotropically aligned NLCs with an additional electric field. In this case the fields that drive the Freédericksz transition and the convection instability, respectively, can be varied independently, which should permit access to a large parameter range of Eqs. (24,25).

For  $H = 0$  and  $\Gamma < 0$  Eqs. (24,25) yield STC at onset. Other examples are the Küppers-Lortz instability in rotating Rayleigh-Bénard convection [119, 120] and systems undergoing a Hopf bifurcation. An example for the latter is the Benjamin-Feir destabilisation mechanism (see e.g. [2]) or the so-called dispersive chaos [19], where a description by a simple Ginzburg-Landau equation should be possible [121]. The origin of chaotic behavior is of course very different in the various systems and their detailed comparison will be fruitful.

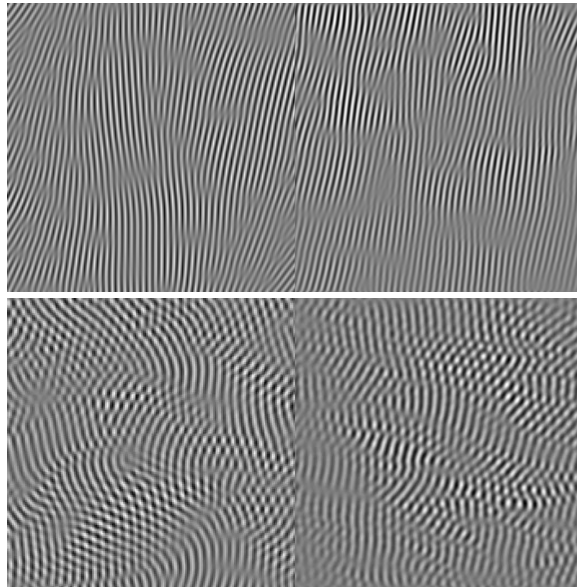


Fig.13 Simulations of Eqs. (24,25) (left) vs. experiment [116] (right) for normal (top) and oblique (bottom) rolls (see text).

## 6 EHC driven by multiplicative noise

### 6.1 Experimental situation and motivation

The influence of stochastic temporal modulation of external parameters in spatially extended systems is an interesting topic of current research [123]. Among the possible effects of the external noise are: shifts of thresholds, the appearance of new bifurcation types, modifications of the bifurcation sequences (e.g. a direct transition towards chaos), or a change from a continuous to hysteretic onset of the pattern-forming instabilities.

The understanding of the various phenomena has been considerably promoted by the investigation of the electrohydrodynamic instabilities in nematic liquid crystals (EHC). The starting point is the common planar configuration (see Fig. 1a), however the applied electric field across the nematic layer is now a superposition of a deterministic component  $E_{det}$  and a stochastic one,  $E_{stoch}$ . In the experiments a low-frequency periodic  $E_{det}$  was used, i.e. in a regime where the deterministic threshold curve as a function of frequency is almost flat (see Fig. 2b). This justifies to use in the theoretical description almost exclusively a time-independent  $E_{det}$  [124, 125, 126, 127, 128, 129, 130, 131, 132, 133, 134, 135, 136, 137, 138, 139, 140], cf. however

[141]. The stochastic field  $E_{stoch}$  is mainly characterized by its strength and the correlation time  $\tau_{stoch}$  of its auto-correlation function.

In the first experiments a 'fast' stochastic component was superimposed [124, 125, 126], then subsequent work was also devoted to 'slow' stochastic driving [127, 128, 129]. Slow and fast refer here to the relation of  $\tau_{stoch}$  to the characteristic times of the liquid crystal, which govern the relaxation of space charge and director in absence of external electric fields.

In these early experiments [124, 125, 126, 127, 128, 129] a highly doped nematic MBBA was used, where the electric conductivity is quite large. It has been demonstrated that adding a fast stochastic field  $E_{stoch}$  with its strength below a certain critical value  $E_c$  leads to a stabilisation of the homogeneous state, i.e. the threshold increases in comparison to a pure deterministic case. However beyond  $E_c$  the stochastic component is destabilizing and a *discontinuous* behaviour of the threshold curve as a function of stochastic-field strength is found (direct transition). With increasing stochastic driving the planforms at the convection threshold changed as well from normal rolls to a grid pattern and finally to a chaotic state (the dynamical scattering mode). The direct transition towards chaos at very high strength of the external noise was described to occur via intermittent bursts of spatially incoherent structures embedded in a homogeneous background [126]. The frequency of the bursts, as well as their duration and the area filled with spatially disordered structures increase with increasing deterministic voltage until the whole cell is filled with a strongly fluctuating spatially disordered structure. The superposition with a slow stochastic field on the other hand would always decrease the deterministic threshold. There were also some indications that the transition might be slightly hysteretic [129, 130]. For a comprehensive review see [129].

In later experiments undoped MBBA (low conductivity) [136, 137] and a different, chemically more stable nematics (Mischung 5) [138] was used. It was at first confirmed that slow external noise was destabilizing, in contrast to a not too strong, fast external noise, which was stabilizing. With increasing strength destabilizing effects take over, i.e. the threshold was eventually found to decrease *continuously* with the strength of the stochastic field.

In these experiments, for pure stochastic driving ( $E_{det} = 0$ ), a new scenario was revealed: With decreasing correlation time a transition from a "conductive" to a "dielectric" regime was observed at a critical  $\tau_{stoch}$ . In the latter regime the threshold was no longer sharp, since stripe pattern would appear and disappears randomly in time [137, 138, 140]. The pattern exhibits a characteristic blinking which corresponds to the phenomenon of *on-off*-intermittency, recently discussed for low-dimensional systems randomly driven just below their threshold of stability, cf. e.g. [142]. The probability distribution for the duration of the laminar phases, i.e., off-periods is governed by a power-law over several orders of magnitude [140].

An important issue for the following is the appropriate description of the

stochastic process. A common approximation is Gaussian white noise, which applies to situations, where the correlation time of the driving stochastic field,  $\tau_{stoch}$ , is kept much shorter than all characteristic time scales in the system. One might argue, that due to the critical-slowing-down the time scale at the onset of EHC is always long, but in fact it turns out that the dynamics of other important processes is not well separated in time from  $\tau_{stoch}$ . Since the system couples to the square of the field strength there is another -more formal- reason which forbids to use a Gaussian white noise: The square of such a process is not a well defined mathematical quantity.

For these reasons the modelling of the stochastic process by a white noise is excluded: One has to use a stochastic model process with finite correlation time, such as the Ornstein-Uhlenbeck process or the dichotomous Markov process. The latter one allows a rigorous treatment of linear problems and can easily be generated in the experiment.

An interesting mathematical problem is posed by the stability of a stochastic trajectory. Different criteria have been discussed in the literature such as the bifurcation of the maximum of the probability density [143], the stability of the first or higher moments [144], or the asymptotic stability of the stochastic trajectory with a probability one (sample stability) [145, 146]. It is plausible that as long as the noise is fast compared to the time scales of the system these stability criteria should give similar results. However, as will be demonstrated for EHC, the correlation time  $\tau_{stoch}$  is not in all cases short. Thus the different criteria give indeed different results except in some limits. Typically, for a fixed noise strength, the tendency towards a destabilisation increases with increasing order of the moments. This feature can be understood, since large but rare fluctuations of a stochastic process are progressively enhanced in the high-order moments. In any case, the sample-stability criterion is consistent with numerical simulations and appears as the natural proper choice [139].

The standard tool to describe the convection instability of the quiescent state is the linear stability analysis. For a deterministic driving voltage the procedure is not difficult to carry through and is well understood (see Sect. 3). However, for stochastic driving already the linear regime presents a strong challenge. Due to the inherent difficulties of the problem further approximations have to be introduced, which amount to a simplified treatment of all convection fields with respect to their vertical ( $z$ -) dependence, which is captured by one single mode. This treatment leads to the so called two-dimensional model [148, 134, 135] and its simplified one-dimensional version [38, 105]. In the case of deterministic driving it has been shown in detail that the exact critical properties can thus be satisfactorily reproduced within a few percent [17, 16].

In the sequel at first the model for stochastically driven EHC is presented (Sect. 6.2), before the criteria for stochastic stability are discussed in Sect. 6.3. The detailed results of the linear analysis in comparison with experiments

are presented in Sect. 6.4. It will turn out, that the theory can explain well a variety of different experimental findings. A discussion of related topics and an outlook to future work can be found in some Concluding remarks.

## 6.2 Modelling of stochastically driven EHC

In the following at first the basic equations and its formal solutions are presented. Furthermore several criteria of stochastic stability are discussed.

**The linearized equations of the two-dimensional model.** The stability investigation of the quiescent state against the formation of normal rolls follows the standard method (see Sect. 3). The anisotropy axis of the system is parallel to  $\mathbf{x}$ , and all field variables vary only in  $x$  and  $z$ . The starting point are the basic equations as discussed in Sect. 2. In the horizontal directions with infinite extent a Fourier transformation (wavenumber  $k_x$ ) is applied; with respect to the transverse direction one Galerkin mode (with wavenumber  $k_z$ ) for each field (velocity, director etc) is used. Their choice is dictated by the boundary conditions at the confining horizontal plates. We have used stress-free boundary conditions, which simplify the calculations and are known to give satisfactory results [17, 149]. The director distortions, the induced space charge, and the quantities  $v_z$ ,  $\partial_z v_x(z)$  have to vanish at the boundaries, where  $v_x$ ,  $v_z$  denote the velocity components parallel and perpendicular to the confining plates, respectively. The velocity field can then be adiabatically eliminated because of the small viscous time scale.

One ends up with a system of two coupled ODE's, which describe the dynamics of the space charge  $q$  and the spatial variation of the angle  $\theta$  between the director and electrode plates,  $\psi = \partial_x \theta$  [148], given as:

$$\dot{\mathbf{z}} = \mathbf{C}(t)\mathbf{z}, \quad (26)$$

where  $\mathbf{z} = (q, \psi)^T$ , and

$$\mathbf{C}(t) = - \begin{pmatrix} 1/T_q & \sigma_H E_t \\ a E_t & \Lambda_1 - \Lambda_2 E_t^2 \end{pmatrix}. \quad (27)$$

The total driving electric field  $E_t = E_{det} + E_{stoch}$  is the superposition of a constant component  $E_{det}$  and a dichotomous Markovian component  $E_{stoch} = E_t^{DMP}$  which takes randomly the values  $\pm E$  and has the autocorrelation  $\langle E_t^{DMP} E_{t'}^{DMP} \rangle = E^2 \exp[-2\nu(t-t')]$ .  $\nu$  determines the inverse correlation time (i.e.  $\tau_{stoch} = 1/2\nu$ ) and describes the mean number of jumps in unit time. One sees immediately that the *square* of the stochastic field enters, which excludes the use of Gaussian white noise as already mentioned in the introduction.

The parameters  $T_q$ ,  $\sigma_H$ ,  $a$ ,  $\Lambda_{1/2}$  are explicitly given by:

$$T_q = \varepsilon_0(\varepsilon_{\parallel} k_x^2 + \varepsilon_{\perp} k_z^2)/(\sigma_{\parallel} k_x^2 + \sigma_{\perp} k_z^2), \quad (28)$$

$$\sigma_H = (\sigma_{\parallel} \varepsilon_{\perp} - \varepsilon_{\parallel} \sigma_{\perp})(k_x^2 + k_z^2)/(\varepsilon_{\parallel} k_x^2 + \varepsilon_{\perp} k_z^2), \quad (29)$$

$$a = \frac{1}{f} \left[ \frac{1}{2} \cdot \frac{(\gamma_1 - \gamma_2)k_x^4 + (\gamma_1 + \gamma_2)k_x^2 k_z^2}{\alpha_1 k_x^2 k_z^2 + (k_x^2 + k_z^2)(\eta_1 k_x^2 + \eta_2 k_z^2)} - \frac{\varepsilon_a k_x^2}{\varepsilon_{\parallel} k_x^2 + \varepsilon_{\perp} k_z^2} \right], \quad (30)$$

$$A_1 = [K_{33} k_x^2 + K_{11} k_z^2] / f, \quad (31)$$

$$A_2 = \varepsilon_0 \varepsilon_a \varepsilon_{\perp} (k_x^2 + k_z^2) / [f(\varepsilon_{\parallel} k_x^2 + \varepsilon_{\perp} k_z^2)]. \quad (32)$$

where  $\eta_{1/2} = [\alpha_4 \mp \gamma_2 + \alpha_5 + \alpha_3] / 2$  are the well-known Miesowicz coefficients constructed from the viscous constants  $\alpha_i, i = 1, 5$  ( $\gamma_1 = \alpha_3 - \alpha_2$ ;  $\gamma_2 = \alpha_3 + \alpha_2$ , see e.g. [17]). For the sake of brevity we have introduced

$$f = \gamma_1 - \frac{1}{4} \cdot \frac{[(\gamma_1 - \gamma_2)k_x^2 + (\gamma_1 + \gamma_2)k_z^2]^2}{\alpha_1 k_x^2 k_z^2 + (k_x^2 + k_z^2)(\eta_1 k_x^2 + \eta_2 k_z^2)}. \quad (33)$$

The coefficients depend on the wavenumber  $k_x$ , which is to be determined by minimizing the threshold voltage. From the vertical boundary condition  $k_z = \pi/d$  holds (odd solutions with  $k_z = 2\pi/d$  play no role like in the deterministic case). Note that both  $1/T_q$  and  $\sigma_H$  are proportional to  $\sigma_{\parallel}$  if  $\sigma_{\parallel}/\sigma_{\perp} = \text{const}$ . The one-dimensional model is readily obtained setting  $k_z = 0$ , i.e. by neglecting the influence of the vertical boundaries. As the characteristic length  $\lambda_x$  of the pattern in the low frequency conduction regime is set by the width of the nematic layer, the 1d theory fails to predict  $\lambda_x$ ; one has to insert  $\lambda_x \approx d$  as a fit parameter to obtain reasonable values for thresholds. However note, that in the high-frequency dielectric regime the critical wavelength becomes an intrinsic bulk property [147, 16] and is already determined within the one-dimensional approach.

For a deterministic driving the undistorted state remains stable against the formation of normal rolls if the solution of (26) converges to zero. For stochastic driving there exist several stability criteria to be discussed below.

**Formal solution.** To obtain a formal solution of Eq. (26) for a given realization of  $E_i^{DMP}$  with jumps at times  $t_{\nu}, \nu = 0, 1, \dots, n$ , where  $t_n > t_{n-1} > \dots > t_1 > t_0$  we first consider a time interval between two jumps where  $\mathbf{C}(t) = \mathbf{C}^{\sigma} = \text{const}, \sigma = \pm$  and diagonalize  $\mathbf{C}^{\sigma}$  by a unitary transformation

$$\mathbf{U}^{\sigma} \mathbf{C}^{\sigma} (\mathbf{U}^{\sigma})^{\perp 1} = \begin{pmatrix} \lambda_1^{\sigma} & 0 \\ 0 & \lambda_2^{\sigma} \end{pmatrix} \equiv \text{diag}(\lambda_i^{\sigma}). \quad (34)$$

Introducing  $\mathbf{W}^{\sigma} = \mathbf{U}^{\sigma} \mathbf{z}$  one finds  $\dot{\mathbf{W}}^{\sigma} = \text{diag}(\lambda_i^{\sigma}) \mathbf{W}^{\sigma}$  which is solved by  $\mathbf{W}^{\sigma}(t) = \text{diag}\{\exp[\lambda_i^{\sigma}(t - t')]\} \mathbf{W}^{\sigma}(t')$ . The inverse transformation leads to

$$\mathbf{z}_{\sigma}(t) = \mathbf{T}^{\sigma}(t - t') \mathbf{z}_{\sigma}(t'), \quad (35)$$

where  $\mathbf{T}^\sigma$  is the time evolution matrix

$$\mathbf{T}^\sigma(\tau) = (\mathbf{U}^\sigma)^{\perp 1} \text{diag}[\exp(\lambda_i^\sigma \tau)] \mathbf{U}^\sigma. \quad (36)$$

For a given realization of the driving process with jumps at the random times  $t_\nu$  iteration of (35) gives the formal solution [139]

$$\mathbf{z}_{\sigma_n}(t) = \mathbf{T}^{\sigma_n}(t - t_n) \cdots \mathbf{T}^{\sigma_1}(t_2 - t_1) \mathbf{T}^{\sigma_0}(t_1 - t_0) \mathbf{z}_{\sigma_0}(t_0). \quad (37)$$

The stability of the stochastic trajectory  $\mathbf{z}_{\sigma_n}(t)$  is determined by the largest Lyapunov exponent  $\lambda_1$  of the product of random matrices in (37) in the limit  $n \rightarrow \infty$ . If this exponent has a positive real part the trajectory diverges, otherwise it converges to zero. The evaluation of infinite products of random matrices is a notorious difficult problem, which appears also in a number of different fields in statistical physics [150] (for further references see e.g. [139]). Eq. (37) is used for the numerical simulations in order to determine stability thresholds (to be compared with analytical results) [139] and also the probability density of the duration of quiescent periods just below the threshold [140].

### 6.3 Stochastic stability criteria

In the following we will present and compare several stability criteria.

**Mean field decoupling.** We first describe a simple approximation [125] which rests on the assumption that the characteristic time of the driving stochastic process is fast compared to all other characteristic times. Then the system will "feel" only the average value of the stochastic field

$$E_t \rightarrow \langle E_t \rangle = E_{det}, \quad E_t^2 \rightarrow \langle E_t^2 \rangle = E_{det}^2 + E^2. \quad (38)$$

This physical picture corresponds to a simple mean-field type decoupling of the averages

$$\langle E_t \mathbf{z} \rangle \rightarrow \langle E_t \rangle \langle \mathbf{z} \rangle. \quad (39)$$

With the above replacements in (27) one obtains from  $\det \mathbf{C} = 0$  the threshold

$$E_{det,th}^2 = \frac{A_1 - A_2 E^2}{\sigma_H a T_q + A_2}, \quad (40)$$

which increases ( $A_2 < 0$ ) in a linear way with the strength of the stochastic field  $E^2$ . In the mean field approximation it is therefore impossible to explain neither the experimentally found discontinuous behaviour of the threshold [126, 127, 128] nor the dependence on the correlation time of the noise [128].

**Stability of moments.** The equations of motions for the first moments form a closed system for  $\langle \mathbf{z} \rangle$  and  $\langle E_t^{DMP} \mathbf{z} \rangle$ . One uses a theorem of Shapiro and Loginov [151]

$$(\partial/\partial t + 2\alpha) \langle E_t^{DMP} \mathbf{z} \rangle = \langle E_t^{DMP} \dot{\mathbf{z}} \rangle, \quad (41)$$

and exploits in addition  $(E_t^{DMP})^2 = E^2 = \text{const}$ . The quantity  $\dot{\mathbf{z}}$  on the RHS of Eq. (41) is replaced by Eq. (26). (Similar equations hold for the higher moments.) The *exact* threshold condition for the stability of moments is nonlinear in the field strength thus opening the possibility for a qualitative (though not quantitative) understanding of the behaviour of the threshold. The standard model in its one-, two- and three-dimensional versions and the 1d model including flexoeffect have been extensively studied within this approach [132, 133, 134, 135].

**Sample stability.** For the following it is crucial that one is able to reduce the complicated dynamics of EHC to a system of two coupled stochastic equations (Eqs. (26)). In that case there exists a standard method to analyze the asymptotic stability of the trajectory (Eq. (37)) for almost all realizations of the driving process (sample stability) [145]. The first step is a transformation from  $(q, \psi)$  to polar coordinates  $(r, \varphi)$ , which leads from (26) to the pair of equations

$$\dot{r} = g(E_t, \varphi)r, \quad (42)$$

$$\dot{\varphi} = h(E_t, \varphi). \quad (43)$$

Equation (43) depends only on  $\varphi$  (the system is skew symmetric) and it is possible to find the stationary solution  $P_\sigma(\varphi)$  of the associated Kolmogorov forward equation for the joint process  $(E_t, \varphi)$

$$\dot{P}_\sigma = \frac{d}{d\varphi}(h_\sigma P_\sigma) - \alpha(P_{\perp\sigma} - P_\sigma), \sigma = \pm, \quad (44)$$

where  $h_\sigma$  is a shorthand notation for  $h(E_\sigma, \varphi)$ . Equation (42) is linear in  $r$  and can be solved for a given trajectory of the driving process. This leads to an expression for the leading Lyapunov exponent [145]

$$\lambda_1 = \lim_{t \rightarrow \infty} \frac{1}{t} \int_0^t d\tau g(E_\tau, \varphi) = \int_{\text{supp}} d\varphi \sum_{\sigma=\pm} P_\sigma(\varphi) g(E_\sigma, \varphi). \quad (45)$$

The second equality holds due to the multiplicative ergodic theorem of Oseledec [152] with *Prob* 1, i.e., for almost all trajectories.

For the nondegenerate (the matrices  $\mathbf{C}^+$  and  $\mathbf{C}^\perp$  do not have an eigenvector in common) and nonrotational (the eigenvalues of  $\mathbf{C}^\sigma$  are real and

distinct) case which is of interest here,  $\lambda_1$  can be found up to quadratures [145]

$$4\lambda_1 = - \sum_{\sigma=\pm} \text{Sp } \mathbf{C}^\sigma - \frac{\int_{\text{supp}} d\varphi F \cdot \frac{d}{d\varphi} \ln |h_+/h_\perp|}{\int_{\text{supp}} d\varphi F/h_+}, \quad (46)$$

where

$$F(\varphi, \varphi_0) = \exp \left[ -\alpha \int_{\varphi_0}^{\varphi} d\varphi \left( \frac{1}{h_+} + \frac{1}{h_\perp} \right) \right], \quad \varphi_0 \in \text{supp}. \quad (47)$$

The two Lyapunov exponents of the system  $\lambda_1 > \lambda_2$  are related by

$$\lambda_1 + \lambda_2 = 1/2 \sum_{\sigma=\pm} \text{Sp } \mathbf{C}^\sigma. \quad (48)$$

For pure stochastic excitation ( $E_{det} \equiv 0$ ), the quadratures in (46) and (47) have been evaluated explicitly in terms of generalized hypergeometric functions both for the 1d [134] and 2d model [139]. Also for a constant, finite field  $E_{det}$  analytical results exist for the 1d model, whereas for the 2d model the integrals in (46) and (47) were evaluated numerically [139].

**Numerical simulations.** The numerical simulation follows trajectories  $\mathbf{z}_{\sigma_n}(t)$  starting from a nonzero but small initial value  $\mathbf{z}(0)$  for a given realization of the driving stochastic process, cf. Eq. (37). A trajectory with  $N$  jumps (corresponding to an average time  $N/\alpha$  with constant  $E_t$  intervals) is considered as diverging if  $\psi = \partial_x \theta \sim k\theta = (\pi\theta)/d > \pi^2/(4d)$ , i.e. for  $\theta > \theta_c \approx \pi/4$ . This critical value for  $\theta$  is chosen, because for  $\theta \gtrsim \pi/4$  the linearization of  $\sin \theta \approx \theta$  on which Eq. 27 is based becomes invalid. The thus determined thresholds are virtually independent of  $N$  and  $\psi_c$  for  $N \gtrsim 10^4$ , i.e. they vary only within a limit of less than one percent when  $N$  and  $\psi_c$  are varied both over a range of several orders of magnitude [139].

In the following the theoretical results are exemplified in detail and also compared with experimental results.

## 6.4 Results

**Comparison of different stability criteria.** The thresholds for the appearance of normal rolls calculated in the one-dimensional model according to the different criteria discussed above are compared in Fig. 14. The total voltage is the superposition of a constant deterministic part ( $U_1 = E_{det}$ ) and a stochastic one ( $U = E_{stoch}$ ) with fast and slow stochastic driving frequency  $\nu$ , respectively. In this part the material parameters are taken in general from [153] (referred to as MBBA I in [139]), but we allow for modifications of the electrical conductivities. The cell thickness is fixed to  $100\mu$  in all calculations.

For small values of the stochastic voltage  $U$  the thresholds from all criteria coincide as must be expected irrespective of  $\nu$ . The insert in Fig.14 addresses the case of slow driving calculated for  $\sigma_{\parallel} = 1.5 \cdot 10^{18} \Omega^{-1} \text{ m}^{-1}$  and  $\sigma_{\parallel}/\sigma_{\perp} =$

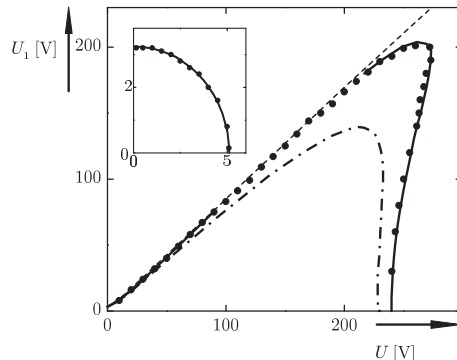


**Fig. 14.** Thresholds for the appearance of normal rolls calculated in the one-dimensional model for a superposition of constant voltage  $U_1$  and a fast stochastic dichotomous voltage  $U$  ( $\nu \simeq 1000 \text{ s}^{-1}$ ). The thresholds are obtained from: mean-field decoupling (dashed line), stability of first moments (dash-dotted line), sample stability (solid line), and numerical simulation ( $\bullet$ ). The insert shows the case of a 'slow' stochastic voltage ( $\nu \simeq 100 \text{ s}^{-1}$ ) for which all criteria (besides the mean field decoupling) give the same result (from [139]; for the material parameters: see text).

1.3. This corresponds to a cut-off frequency  $f_d \approx 62 \text{ Hz}$  in the case of an applied deterministic ac voltage, which is comparable with  $\nu = 100 \text{ Hz}$ . The results for fast driving are shown (for  $\sigma_{\parallel} = 6 \cdot 10^{19} \Omega^{-1} \text{ m}^{-1}$  and  $\sigma_{\parallel}/\sigma_{\perp} = 1.3$ ) are shown in more detail. The stochastic frequency is now much larger than the corresponding cut-off frequency  $f_d = 26 \text{ Hz}$ . For a wide range of  $U$  the threshold from the mean field decoupling is very close to that of the sample stability, but for  $U$  beyond the threshold ( $\approx 240 \text{ V}$ ) for pure stochastic excitation ( $U_1 = 0$ ) they are drastically different.

The results can be understood through an comparison of the characteristic times of the system and of the noise, cf. Fig. 15. The characteristic times of the stochastically driven system are given by the modulus of the inverse of the Lyapunov exponents  $\lambda_1$  and  $\lambda_2$ . At the threshold we have  $\lambda_1 = 0$ , the corresponding time  $\tau_1$  diverges and is thus well separated from  $\tau_{stoch}$ . The second characteristic time for the electric fields at the threshold can be determined exactly [139]

$$\tau_2 = |1/\lambda_2| = (1/T_q + \Lambda_1 - \Lambda_2(E_{det}^2 + E^2))^{-1}, \quad (49)$$

it decreases with increasing values of the threshold fields and may reach the order of  $\tau_{stoch}$ . In this case the mean-field decoupling is not justified and the threshold obtained from the stability of the moments differs quantitatively from the sample-stability threshold. If instead  $\tau_{stoch}$  is clearly separated from

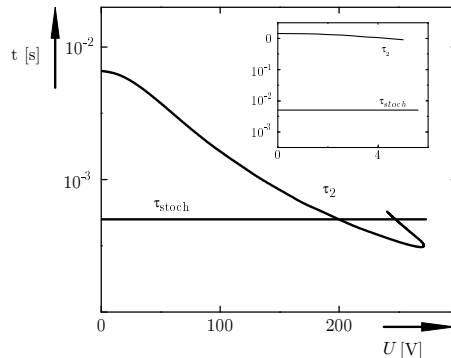


**Fig. 15.** The characteristic time  $\tau_2 = |1/\lambda_2|$  at the sample stability threshold shown in 14 decreases with increasing voltage [139]. The initially clearly separated time scales of  $\tau_2$  and  $\tau_{stoch} = 1/2\nu$  become of the same order at sufficiently high stochastic voltage. The insert shows the case where the time scales are well separated.

at least one of the characteristic times of the system, both moment's and sample stability criteria give similar results, see inserts in Figs. 14 and 15. The numerical simulations confirm the results obtained from the criterion of sample stability, which was therefore used in [139, 140].

The region describing the stability of the moments is always smaller than that for sample stability since the divergence of the trajectories is sufficient for the divergence of the moments: For large times one finds

$$r_t = e^{\langle \lambda[E_r] \rangle t} \leq \langle e^{\lambda[E_r]t} \rangle = \langle r_t \rangle, \quad (50)$$

where the inequality holds due to the convexity of the exponential function. Finally one should mention that the thresholds for stochastic excitation are always below that for deterministic excitation (for otherwise identical parameters and wave numbers). This is plausible since generally the thresholds increase with the increasing frequency and a stochastic trajectory with a given mean number of jumps always contains lower Fourier components.

**Pure stochastic excitation.** The stability diagram for pure stochastic excitation shows a topological difference between 'slow' and 'fast' driving, cf. Fig. 16. In the former case we have an unstable island in the left lower corner of Fig. 16a. The corresponding mode (low threshold and small wavenumber) is called *conductive*. With increasing mean frequency  $\nu$  of the driving field this island shrinks continuously. There is a sharp transition if it disappears: The instability is now towards a mode with a higher threshold and a much larger wave number as it is typical for the *dielectric* regime, cf. Fig. 16b.

We remark that also for deterministic driving the stability diagram has analogous properties. Note, that the different temporal symmetries of dielectric and conductive mode in the deterministic case (see Sect. 3) are not crucial here.

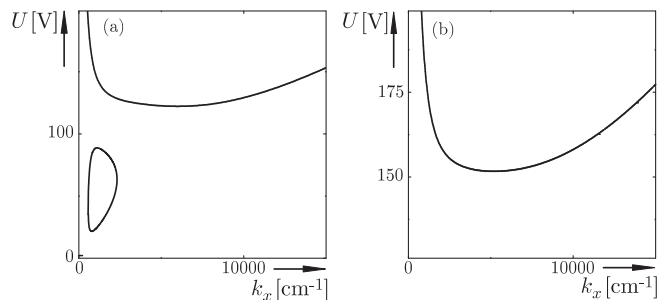


**Fig. 16.** Mode selection for pure stochastic excitation [139]. Shown are the neutral curves for the two-dimensional model in (a) the conductive regime ( $\nu = 100 \text{ s}^{-1}$ ) and in (b) the dielectric regime ( $\nu = 400 \text{ s}^{-1}$ ). The unstable region in the left lower corner of (a) corresponds to the conductive mode and shrinks with increasing mean frequency of the driving process and is then absent in the dielectric regime (b).

The “critical” wave number  $k_x$  increases as function of the mean frequency  $\nu$  with a slope much smaller than for deterministic driving. This is also found in experiments [138], cf. Fig. 17, and can be qualitatively understood by an argument similar to that given above according to which stochastic driving contains always contributions of lower Fourier modes.

For stochastic driving one observes in the region indicated in Fig. 17 by open rectangles phenomena which resemble *on-off*-intermittency: Normal roll patches appear and disappear in an irregular way at voltages already below the sample stability threshold [137, 138, 140]. The frequency of the bursts increases with the strength of the stochastic field, their duration depends on the characteristic time  $\tau_{stoch}$  of the noise. Since the undistorted state is well described by the linear theory this phenomenon can be captured by simulations based on Eq. (37). We have found when approaching the threshold ( $\lambda_1 = 0$ ) from below that the probability distribution for the duration  $\tau_{off}$  of the undistorted state (i.e the laminar or off-periods) is governed by a power-law  $p(\tau_{off}) \sim \tau_{off}^{-3/2}$  over several orders of magnitude, in good agreement with the experiment [140].

**Superposition of deterministic and stochastic field.** The superposition of a deterministic voltage  $U_1$  with a ‘fast’ stochastic voltage  $U$  with increas-

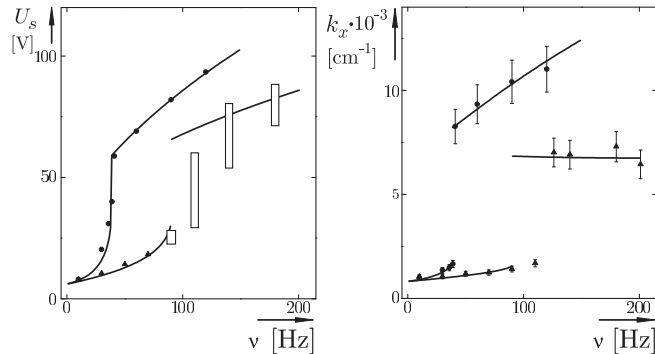


**Fig. 17.** Theory versus experiment: Thresholds and selected wave numbers of normal rolls depending on the (mean) frequency of the driving field [138]. As explained in the text, the curves for stochastic driving are always below those for deterministic driving. Experimentally determined thresholds ( $\bullet$  deterministic driving, triangles: stochastic driving) are compared with those obtained from the two-dimensional theory (sample stability criterion for the stochastic case). The experiment is performed with the nematic “Mischung 5”. The open rectangles indicate the range where for stochastic driving phenomena were observed which resemble *on-off*-intermittency (see text).

ing strength stabilizes at first the undistorted state. This is shown in Fig. 18, where the threshold increases initially with increasing  $U$ . This remains true up to a certain “critical” value of  $U$  beyond which the threshold curve bends down ( $U$  becomes destabilizing). The threshold curves are determined experimentally following a suitable protocol involving changes in  $U, U_1$  inside the stable regime until a point on the linear stability curve is hit.

The region where the undistorted state is stable *may* extend beyond the threshold values of deterministic or stochastic driving alone, thus forming a stable tongue in the  $U-U_1$  plane (i.e. the upper curve in Fig. 18 bends back at large  $U$ ). This explains why in experiments [126, 127, 128, 129] a discontinuous behaviour of the threshold was observed, when a stochastic voltage  $U$  of a given strength was applied first and then the deterministic voltage  $U_1$  was increased up to the instability of the homogeneous phase. In other words, below a certain value  $U_c$  ( $\approx 230$ V in Fig. 18) the threshold is found at a finite deterministic voltage  $U_{1th}$ , whereas for  $U > U_c$  convection sets in immediately at  $U_{1th} = 0$ .

The appearance of the stable tongue depends on the material parameters. Roughly speaking, the tendency towards its formation decreases with increasing Helfrich parameter  $\zeta^2$  (independent of the stability criterion, i.e. for moment’s stability [132] as well as for sample stability [139]). The Hel-

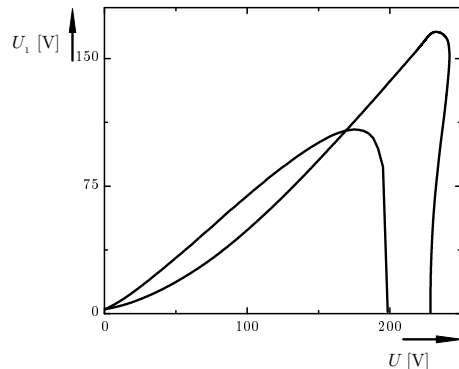


**Fig. 18.** Comparison of sample stability thresholds for different values of the conductivity at fixed  $\nu = 1000\text{s}^{-1}$  in the one-dimensional model [139]. The tendency towards formation of a stable tongue increases with increasing conductivity. Shown are the cases  $\sigma_{\parallel} = 1.11 \cdot 10^{11} \Omega^{-1} \text{cm}^{-1}$  and  $\sigma_{\parallel} = 2.22 \cdot 10^{11} \Omega^{-1} \text{cm}^{-1}$ ,  $\sigma_{\parallel}/\sigma_{\perp} = 1.5$ . In the latter case there is a stable tongue so that, following the measuring procedure described in the text, the threshold curve appears discontinuous. The mean number of jumps is  $\nu = 1000\text{s}^{-1}$  (Material parameters MBBA II from [148, 139]).

frich parameter (which alone determines  $f_d$  in units of the charge relaxation time  $\tau_q$  (see Eq. (12)) depends only on the ratio  $\sigma_{\parallel}/\sigma_{\perp}$ . A further important parameter is in fact the absolute value of the conductivity  $\sigma_{\parallel}$  which may differ from sample to sample considerably and which can be changed easily by doping. The tendency towards formation of a stable tongue increases with increasing  $\sigma_{\parallel}$  while  $\sigma_{\parallel}/\sigma_{\perp}$  is kept constant (cf. Fig. 18). Note that  $f_d \sim \sigma_{\parallel}$  in physical units.

The early experiments [126, 127, 128, 129] were performed presumably with highly doped MBBA ( $f_d = 360\text{Hz}$  in [129]). In later experiments with undoped MBBA [136, 137] ( $f_d \approx 170\text{Hz}$ ) and a different, chemically more stable nematics (*Mischung 5*) [138] no stable tongue and correspondingly no discontinuous behaviour of the threshold was found.

As already mentioned the superposition of a deterministic field with a 'slow' stochastic one leads always to a monotonous decrease of the threshold with increasing stochastic field (see insert in Fig. 14) in agreement with experiments.

The difference of the thresholds for the one-dimensional and two-dimensional versions of the standard model are in general small. The selected wave numbers, however, differ significantly, cf. Fig. 19. This is evident, since  $k_x$  is always chosen to be  $\pi/d$  in the one-dimensional version, whereas it increases in fact with increasing strength of the stochastic field. This is consistent with

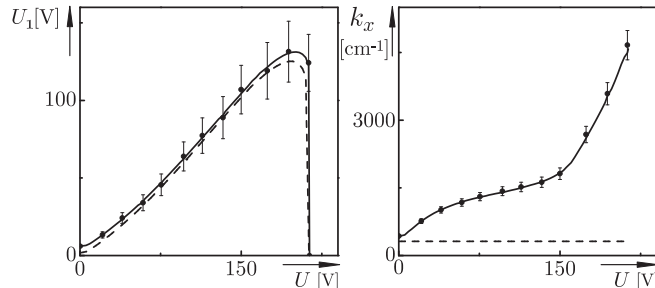


**Fig. 19.** Thresholds and selected wave numbers for the superposition of a constant voltage  $U_1$  with a stochastic dichotomous voltage  $U$  obtained for the one-dimensional (dashed line) and the two-dimensional model (solid line) from the sample stability criterion and from numerical simulation (●) [139]. Material parameters from [148],  $\nu = 1000 \text{ s}^{-1}$ .

experimental findings [136, 137, 138]. A detailed quantitative comparison of two-dimensional theory and experiment is in preparation.

### 6.5 Concluding remarks and outlook

The theoretical treatment presented in this review has obviously the capability for a convincing explanation of a variety of experimental findings. This has been demonstrated for the following phenomena: (i) The discontinuous behaviour of the threshold at a critical strength of the noise, (ii) the change from discontinuous to continuous behaviour of the threshold with increasing correlation time of the noise, (iii) the change from continuous to discontinuous behaviour of the threshold with increasing conductivity, (iv) the change from stabilizing to destabilizing effect of the noise if its correlation time becomes comparable to the correlation time of the system, and (v) the on-off intermittency observed in very recent experiments. In the following we will mention some issues that certainly need further investigation.

In the numerical simulations of the two-dimensional model it was observed that the fluctuations in the distribution of Lyapunov exponents for trajectories of finite length (which mean fluctuations of the threshold) increase if the characteristic times of noise and system become comparable, cf. Fig. 19. Fluctuations of thresholds were also observed in experiment for sufficiently large noise [136, 137, 138, 140]. The theoretical treatment of these fluctuations leads to the problem of generalized Lyapunov exponents [150, 154].

The conductivity enters the standard model considered here as a material parameter. Recently, Treiber and Kramer [33] have developed a more sophisticated model (WEM, see Sect. 4.2), where ionic migration, diffusion

and dissociation-recombination processes are included. Thus the electric conductivity becomes a variable which introduces new time and length scales. In the deterministic case the primary bifurcation phenomena become much richer (Hopf, subcritical), and the analysis of stochastic driving within this model will be certainly rewarding.

In the present work the stability of the undistorted state against *one* mode describing roll patterns of a fixed wave number was considered. If the characteristic time of the noise is of the order of the inverse growth rate of a typical mode, the process of mode selection will not be completed until the next jump of the noise. Thus a band of wave numbers might be involved. This could lead to a sort of dynamical pattern as observed in experiments. At least in a conceptually different system (of Hamiltonian or dissipative gradient type) it has been recently shown, that a continuous band of wave numbers might remain relevant for the long-time behaviour [162].

The inherent difficulties of stochastically driven EHC substantially increase if it comes to the description of the nonlinear regime. A numerical treatment of the full set of nonlinear electrohydrodynamic equations seems at present not to be feasible even in the deterministic case. However, a reliable description is possible in the weakly nonlinear regime in terms of order parameter equations (see Sect. 3). The general problem of systematically deriving amplitude equations in the stochastic case has been addressed in few investigations, see e.g. [157, 158, 159, 160, 161]. However, it is an open question, which approach applies to the case of multiplicative noise in EHC with not always well separated time scales and finite correlation time of the noise. One might speculate that for sufficiently fast driving a kind of order parameter equations with “averaged” coefficients could result, while in the opposite case the coefficients might be stochastic quantities. One should also be aware of the fact, that a deterministic supercritical bifurcation can change to a subcritical one under the influence of noise [155, 156].

At the moment nonlinear partial differential equations, e.g. of Ginzburg-Landau or Swift-Hohenberg type, with additive or multiplicative Gaussian white noise (*introduced ad hoc*) are a subject of intense studies [163, 164, 165, 166, 167, 168, 169, 170, 171, 172, 173, 174]. In this context, Becker and Kramer [175, 176] found a controllable approximation to determine the threshold of sample stability without knowledge of the stationary distribution. A zero-dimensional version, the Stratonovich model, was solved rigorously for Gaussian white noise [177, 178] and dichotomous noise [179]. More recently, a 1d model with multiplicative noise that is a product of a Gaussian white noise in time and a spatial periodic function was considered [180].

Here we have concentrated on the case of stochastically driven electrohydrodynamic convection, i.e. a multiplicative, parametric, external noise. One should note that the very interesting and intriguing problem of thermal fluctuations, i.e. the case of additive, internal noise has also motivated many experimental and theoretical activities [24].

## 7 General Conclusions

In this review we have described to some extent the present status of research in EHC. In near future it is to be expected, that the combined application of electric and magnetic fields will be explored in more detail. Any additional control parameter is obviously very useful to unfold bifurcation scenarios and to accentuate specific mechanism (for a recent example see [181]). But also very unexpected and not yet understood phenomena can show up like the dendritic growth of EHC patterns (see [182]). Many other problems ask for further investigation. Among them are the properties of the abnormal rolls, in particular the defect and wall structures in this state, which certainly determine the patterns not too far from threshold. EHC is a nice paradigm for the formation of chevrons, i.e. an super-structure of particle-like defects, which develops out of a gas of “free” defects. The formation of defect chains is also observed in other cases for instance in simulations of the complex Ginzburg-Landau equation [183].

Another issue is the characterization of spatial temporal chaos (STC), which is the subject of current research in general. STC can easily be produced in EHC experiments by increasing the driving voltage. The system is apparently well suited to study such statistical issues, because of the short characteristic times and large aspect ratios. For example it has been stressed recently that time-averages of the patterns unlike a single snapshot might contain useful information about characteristic times and length of a system [184] as function of the control parameter. This has been confirmed in recent experimental studies [185], where the transition and the possible origin of the STC has been characterized.

Furthermore one should keep in mind, that typical bifurcation scenarios in EHC can be found as well in RBC of nematics [186]. It is for instance easy to find a Hopf bifurcation at threshold in the homeotropic case (for recent experiments see e.g. [187]). The close analogy between EHC and RBC is also reflected in the theoretical analysis [56].

Though not directly related, one should mention finally that interesting instabilities in nematics can also appear under the influence of shear flow [188]. Then a viscous torque is exerted on the director, which was part of the destabilisation loop in EHC, where the director is situated in the shear plane. The flow instabilities in this geometry are currently under investigation, under the application of oscillatory flows. The scenarios are unexpectedly rich. One finds spatially homogeneous oscillations of the director in Couette flow [189] as well as the bifurcation to convection-roll patterns under Poiseuille flow [190].

**Acknowledgements** We have benefitted a lot from discussions with G. Ahlers, H. Brand, A. Buka, S. Kai, I. Rehberg and W. Zimmermann. Exceptional is the role of L. Kramer, who has been always strongly involved in the

many aspects of EHC, which have been discussed in this review. Crucial for any scientific progress is the effort of motivated coworkers. We are in particular indebted to H. Amm, W. Decker, A. Hertrich, Th. John, A. Lange, R. Müller, E. Plaut, A. Rossberg and M. Treiber. They and G. Ahlers, A. Buka, I. Rehberg have also kindly provided graphs of their results. We are grateful to F. Schmoegner for his help preparing the manuscript.

## References

- 1 P. Manneville, *Dissipative Structures and Weak Turbulence*, Academic Press, (New York 1990).
- 2 M. C. Cross and P. C. Hohenberg, *Rev. Mod. Phys.* **65**, 851 (1993).
- 3 F. H. Busse, Fundamentals of thermal convection, in W. R. Peltier, editor, *Mantle convection, Plate Tectonics and Global Dynamics*, page 23, Gordon and Breach, (1989).
- 4 P. de Gennes and J. Prost, *The Physics of Liquid Crystals*, Clarendon Press, (Oxford 1993).
- 5 S. Chandrasekhar, *Liquid Crystals*, University Press, (Cambridge 1992).
- 6 A. Buka and e. L. Kramer, *Pattern formation in liquid crystals*, Springer-Verlag, (New York 1995).
- 7 E. Dubois-Violette, G. Durand, E. Guyon, P. Manneville, and P. Pieranski, Instabilities in nematic liquid crystals, in L. Liebert, editor, *Solid state physics, Suppl. 14*, page 147, Academic Press, New York, (1978).
- 8 L. M. Blinov, *Electrooptical and Magnetooptical Properties of Liquid Crystals*, John Wiley, (New York 1983).
- 9 S. A. Pikin, *Structural Transformations in Liquid Crystals*, Gordon and Breach Science Publishers, (New York 1991).
- 10 I. Rehberg, B. L. Winkler, M. de la Torre, S. Rasenat, and W. Schöpf, *Adv. Solid State Physics* **29**, 35 (1989).
- 11 S. Kai and W. Zimmermann, *Prog. Theor. Phys. Suppl.* **99**, 458 (1989).
- 12 L. Kramer, E. Bodenschatz, W. Pesch, W. Thom, and W. Zimmermann, *Liquid Crystals* **5**(2), 699 (1989).
- 13 W. Zimmermann, *MRS Bulletin* **XVI**, 46 (1991).
- 14 S. Kai, *Forma* **7**, 189 (1992).
- 15 L. Kramer and W. Pesch, *Annu. Rev. Fluid Mech.* **27**, 515 (1995).
- 16 L. Kramer and W. Pesch, Electrohydrodynamic instabilities in nematic liquid crystals, in A. Buka and L. Kramer, editors, *Pattern formation in liquid crystals*, Springer, (New York 1995).
- 17 E. Bodenschatz, W. Zimmermann, and L. Kramer, *J. Phys.(Paris)* **49**, 1875 (1988).
- 18 M. Treiber, N. Eber, Á. Buka, and L. Kramer, *J. Phys. France II* **7**, 649–661 (1997).
- 19 M. Dennin, G. Ahlers, and D. Cannell, Measurement of material parameters of the nematic crystal i52, in P. Cladis and P. Palfy-Muhoray, editors, *Spatio-temporal patterns in nonequilibrium complex systems*, Santa Fe Institute Studies in the Sciences of Complexity **XXI**, Addison-Wesley, New York, (1994).
- 20 M. Dennin, D. Cannell, and G. Ahlers, *Mol. Cryst. Liq. Cryst.* **261**, 337 (1995).

- 21 M. Dennin, G. Ahlers, and D. S. Cannell, Phys. Rev. Lett. **77**, 2475 (1996).
- 22 H. R. Brand, C. Fradin, P. L. Finn, W. Pesch, and P. E. Cladis, Physics Lett. A **235**, 508 (1997).
- 23 I. Rehberg, S. Rasenat, M. de la Torre Juarez, W. Schöpf, F. Hörner, G. Ahlers, and H. Brand, Phys.Rev.Lett **67**, 596 (1991).
- 24 M. Treiber, Thermal fluctuations in pattern forming instabilities, in A. Buka and L. Kramer, editors, *Pattern formation in liquid crystals*, Springer, (New York 1995).
- 25 M. J. Stephen and J. P. Straley, Rev. Mod. Phys. **46**, 617 (1974).
- 26 H. Pleiner and H. Brandt, Hydrodynamics and electrohydrodynamics of liquid crystals, in A. Buka and L. Kramer, editors, *Pattern formation in liquid crystals*, Springer, (New York 1995).
- 27 F. M. Leslie, Quart. J. Mech. Appl. Math. **19**, 357 (1966).
- 28 O. Parodi, J. Phys. (Paris) **31**, 581 (1970).
- 29 F. H. Busse and E. W. Bolton, J. Fluid Mech. **146**, 115 (1984).
- 30 R. B. Meyer, Phys. Rev. Lett. **22**, 918 (1969).
- 31 N. Madhusudana and G. Durand, J. Phys.Paris **46**, L195 (1985).
- 32 W. Decker, PhD thesis, Universität Bayreuth, (1995).
- 33 M. Treiber and L. Kramer, Mol. Cryst. Liq. Cryst. **261**, 311 (1995).
- 34 A. C. Newell, T. Passot, and J. Lega, Annu. Rev. Fluid Mech. **25**, 399 (1993).
- 35 G. Dangelmayr and L. Kramer, in F. Busse and A. Müller, editors, *this volume*, Springer, (New York 1998).
- 36 W. Pesch and L. Kramer, General mathematical description of pattern forming instabilities, in A. Buka and L. Kramer, editors, *Pattern formation in liquid crystals*, Springer, (New York 1995).
- 37 Orsay Liquid Crystal Group, Phys. Rev. Lett. **26**, 1642 (1970).
- 38 E. Dubois-Violette, P. G. de Gennes, and O. J. Parodi, J. Phys.(Paris) **32**, 305 (1971).
- 39 H. Haken, *Synergetics*, Springer-Verlag, (1978).
- 40 M. C. Cross, Phys. Fluids **23**, 1727 (1980).
- 41 Q. Feng, W. Pesch, and L. Kramer, Phys. Rev. A **45**, 7242 (1992).
- 42 Q. Feng, W. Decker, W. Pesch, and L. Kramer, J. Phys. France **II**, 1303 (1992).
- 43 M. Kaiser and W. Pesch, Phys. Rev. E **48**, 4510 (1993).
- 44 V. Ginzburg and L. Landau, Zh.Eksp.Teor.Fiz. **20**, 1064 (1950).
- 45 W. Pesch and L.Kramer, Z.Phys. B **63**, 121 (1986).
- 46 L. Kramer, E. Bodenschatz, W. Pesch, and W. Zimmermann, in W. Güttinger and G. Dangelmayr, editors, *The Physics of Structure Formation*, Springer, (Berlin 1987).
- 47 E. Bodenschatz, M. Kaiser, L. Kramer, W. Pesch, A. Weber, and W. Zimmermann, Patterns and defects in liquid crystals, in P. Coulet and P. Huerre, editors, *New Trends in Nonlinear Dynamics and Pattern Forming Phenomena: The Geometry of Nonequilibrium*, Plenum Press, (1990). NATO ASI Series.
- 48 A. C. Newell and J. A. Whitehead, J. Fluid Mech. **38**, 279 (1969).
- 49 L. A. Segel, J. Fluid Mech. **38**, 203 (1969).
- 50 A. Buka and L. Kramer, Theory of transient patterns in the splay fredericksz transition of nematics, in S. Kai, editor, *Pattern formation in complex dissipative systems*, World Scientific, (Kitakyushu, Japan 1991).

- 51 W. Decker and W. Pesch, *J.Phys.II France* **4**, 493 (1994).
- 52 A. G. Rossberg, A. Hertrich, L. Kramer, and W. Pesch, *Phys. Rev. Lett.* **76**, 4729–4732 (1996).
- 53 M. I. Tribelsky and K. Tsuboi, *Phys. Rev. Lett* **76**, 1631 (1996).
- 54 H. Riecke, *Phys. Rev. Lett.* **68**, 301 (1992).
- 55 H. Riecke and G. D. Granzow, to appear in *Phys. Rev. Lett.*, (1998).
- 56 E. Plaut and W. Pesch, to appear in *Phys. Rev. E* (1998).
- 57 H. Zhao and L. Kramer. in preparation, (1998).
- 58 H. Zhao, L. Kramer, I. Rehberg, and A. Rudroff. submitted to *Phys. Rev. Lett*, (1998).
- 59 E. F. Carr, *Mol. Cryst. Liq. Cryst.* **7**, 253 (1969).
- 60 W. Helfrich, *J. Chem. Phys.* **51**, 4092 (1969).
- 61 R. Ribotta and A. Joets, Defects and interactions with the structure in ehd convection in nematic liquid crystals, in J. E. Wesfreid and S. Zaleski, editors, *Cellular Structure in Instabilities*, page 249, Springer, (Berlin 1984).
- 62 A. Joets and R. Ribotta, *J. Phys.(Paris)* **47**, 595 (1986).
- 63 S. Kai and K. Hirakawa, *Prog. Theor. Phys. Suppl.* **64**, 212 (1978).
- 64 S. Kai, N. Chizumi, and M. Kohno, *Phys. Rev. A* **40**, 6554 (1989).
- 65 S. Kai. unpublished, (1988).
- 66 A. Joets and R. Ribotta, *Phys. Rev. Letters* **60**, 2164 (1988).
- 67 I. Rehberg, S. Rasenat, and V. Steinberg, *Phys. Rev. Lett.* **62**, 756 (1989).
- 68 I. Rehberg, S. Rasenat, M. de la Torre-Juarez, and V. Steinberg, *Phys. Rev. Lett.* **61**, 2448 (1988).
- 69 M. Treiber, *On the Theory of the Electrohydrodynamic Instability in Nematic Liquid Crystals near Onset*, PhD thesis, Universität Bayreuth, (1996).
- 70 M. Lowe and J. Gollub, *Phys.Rev.Lett* **55**, 2575 (1985).
- 71 S. Rasenat, E. Braun, and V. Steinberg, *Phys. Rev. A* **42**, 5728 (1991).
- 72 S. Nasuno and S. Kai, *Europhys. Lett.* **14**(8), 779 (1991).
- 73 S. Nasuno, S. Takeuchi, and Y. Sawada, *Phys. Rev.* **A40**, 3457 (1989).
- 74 G. Goren, I. Procaccia, S. Rasenat, and V. Steinberg, *Phys. Rev. Lett.* **63**, 1237 (1989). It appears that there is no merit to the theory presented in this paper, see L. Kramer, E. Bodenschatz and W. Pesch, *Phys. Rev. Lett.* **64**, 2588 (1990)
- 75 S. Rasenat, V. Steinberg, and I. Rehberg, *Phys. Rev. A* **42**, 5998 (1990).
- 76 E. Braun and V. Steinberg, *Europhys. Lett.* **15**(2), 167 (1991).
- 77 W. Pesch, W. Decker, Q. Feng, M. Kaiser, L. Kramer, and A. Weber, Weakly nonlinear analysis of pattern formation in nematic liquid crystals, in J. M. Coron, F. Helein, and J. M. Ghidaglia, editors, *Nematics: Mathematical and Physical Aspects*, page 291, Kluwer Academic Publishers, (Dordrecht 1991). NATO ASI Series.
- 78 M. Kaiser, W. Pesch, and E. Bodenschatz, *Physica D* **59**, 320 (1992).
- 79 S. Sasa, *Prog. Theor. Phys.* **83**, 824 (1990).
- 80 S. Sasa, *Prog. Theor. Phys.* **84**, 1009 (1990).
- 81 E. Braun, S. Rasenat, and V. Steinberg, *Europhys. Lett.* **15**, 597 (1991).
- 82 S. Nasuno, O. Sasaki, S. Kai, and W. Zimmermann, Stability diagram in electrohydrodynamic convection of nematics electrohydrodynamic convection in nematics: the homeotropic case, in S. Kai, editor, *Pattern formation in complex dissipative systems and Global Dynamics*, page 275, World scientific, (1992).

- 83 E. Plaut, W. Decker, A. Rossberg, L. Kramer, and W. Pesch, Phys. Rev. Lett. **79**, 2376, (1997).
- 84 H. Richter, A. Buka, and I. Rehberg, in P. Cladis and P. Palffy-Muhoray, editors, *Spatio-temporal patterns in nonequilibrium complex systems*, Santa Fe Institute Studies in the Sciences of Complexity **XXI**, Addison-Wesley, New York, (1994).
- 85 M. Dennin, M. Treiber, L. Kramer, G. Ahlers, and D. Cannell, Phys. Rev. Lett. **76**, 319 (1996).
- 86 M. Treiber and L. Kramer, to appear in Phys. Rev. E (1998).
- 87 W. Zimmermann and L. Kramer, Phys. Rev. Lett. **55**, 402 (1985).
- 88 M. Dennin, G. Ahlers, and D. S. Cannell, Science **272**, 388 (1997).
- 89 E. Moses, J. Fineberg, and V. Steinberg, Phys. Rev. A **35**, 2757 (1987).
- 90 R. Heinrichs, G. Ahlers, and D. S. Cannell, Phys. Rev. A **35**, 2761 (1987).
- 91 S. Fauve, S. Douady, and O. Thual, J. Phys.(Paris) **II 1**, 311 (1991).
- 92 R. Deissler and H. Brand, Phys. Rev. A **44**, R3411 (1991).
- 93 R. Deissler and H. Brand, Physica D **117**, 95 (1998).
- 94 Y. Tu, Phys. Rev. E **56**, R6554 (1997).
- 95 U. Bisang and G. Ahlers, Phys.Rev.Lett **80**, 3061 (1998).
- 96 M. Dennin, D. S. Cannell, and G. Ahlers, Phys. Rev. E **57**, 638 (1997).
- 97 H. Riecke and L. Kramer, submitted to Physica D (1998).
- 98 A. Joets and R. Ribotta, J. Stat. Phys. **64**, 981 (1991).
- 99 X. Yang, A. Joets, and R. Ribotta, in J. E. Wesfried, H. R. Brand, P. Manneville, G. Albinet, and N. Boccara, editors, *Propagation in Systems far from Equilibrium*, Springer, (Berlin 1988).
- 100 R. Ribotta, A. Joets, and L. Lin, Phys. Rev. Lett. **56**, 1595 (1986).
- 101 F. H. Busse, Rep. Prog. Phys. **41**, 1929 (1978).
- 102 S. Nasuno, O. Sasaki, S. Kai, and W. Zimmermann, Phys. Rev. A **46**, 4954 (1992).
- 103 H. Amm, R. Stannarius, and A. G. Rossberg, submitted to Physica D (1998).
- 104 A. Lindner, A. G. Rossberg, and L. Kramer. in preparation.
- 105 I. Smith, Y. Galerne, S. Lagerwall, E. Dubois-Violette, and G. Durand, J. Phys. Colloq. France **36**, C1-237 (1975).
- 106 P. Tóth, Á. Buka, J. Peinke, and L. Kramer, Phys. Rev. E (1997, submitted).
- 107 U. Schneider, M. de la Torre-Juarez, W. Zimmermann, and I. Rehberg, Phys. Rev. A **46**, 1009 (1992).
- 108 M. Scheuring, L. Kramer, and J. Peinke, Phys. Rev. E (1998, submitted).
- 109 S. Kai, Y. Adachi, and S. Nasuno, Stability diagram, defect turbulence, and new patterns in electroconvection in nematics, in P. E. Cladis and P. Palffy-Muhoray, editors, *Spatio-Temporal Patterns in Nonequilibrium Complex Systems*, Addison-Wesley Publishing Company, (1994). SFI Studies in the Sciences of Complexity.
- 110 A. G. Rossberg and L. Kramer, Physica D **submitted** (1997).
- 111 A. Rossberg, PhD thesis, Universität Bayreuth, (1997).
- 112 A. Hertrich, PhD thesis, Universität Bayreuth, (1995).
- 113 L. Kramer, A. Hertrich, and W. Pesch, Electrohydrodynamic convection in nematics: the homeotropic case, in S. Kai, editor, *Pattern formation in complex dissipative systems and Global Dynamics*, page 238, World scientific, (1992).
- 114 A. Hertrich, W. Decker, W. Pesch, and L. Kramer, J. Phys. France **II 2**, 1915 (1992).

- 115 H. Richter, N. Klöpper, A. Hertrich, and A. Buka, *Europhys. Lett.* **30**, 37 (1995).
- 116 H. Richter, A. Buka, and I. Rehberg. unpublished.
- 117 S. Kai, K. Hayashi, and Y. Hidaka, *J. Phys. Chem.* **100**, 19007 (1996). A
- 118 S. Kai, K. Hayashi, and Y. Hidaka, preprint (1997).
- 119 G. Küppers and K. Lortz, *J. Fluid Mech.* **35**, 609 (1996).
- 120 Y. Hu, R. E. Ecke, and G. Ahlers, *Phys. Rev. Lett.* **74**, 5040 (1995).
- 121 P. Kolodner, S. Slimani, N. Aubry, and R. Lima, *Physica D* **85**, 165 (1995).
- 122 L. Kramer, E. Bodenschatz, and W. Pesch, *Phys. Rev. Lett.* **64**, 2588 (1990).
- 123 *Noise in nonlinear dynamical systems*, Vols. 1-3, edited by F. Moss and P. V. E. McClintock (Cambridge University Press, Cambridge, 1989).
- 124 S. Kai, T. Kai, M. Takata, and K. Hirakawa, *J. Phys. Soc. Jpn.* **47**, 1379 (1979).
- 125 T. Kawakubo, A. Yanagita, and S. Kabashima, *J. Phys. Soc. Jpn.* **50**, 1451 (1981).
- 126 H. R. Brand, S. Kai, and S. Wakabayashi, *Phys. Rev. Lett.* **54**, 555 (1985).
- 127 S. Kai, T. Tamura, S. Wakabayashi, M. Imasaki, and H. R. Brand, *IEEE-IAS Conf. Records* **85CH**, 1555 (1985).
- 128 S. Kai, H. Fukunaga, H. R. Brand, *J. Phys. Soc. Jpn.* **56**, 3759 (1987).
- 129 S. Kai, H. Fukunaga, H. R. Brand, *J. Stat. Phys.* **54**, 1133 (1989).
- 130 S. Kai, in: Ref. [123], 22-76.
- 131 H. R. Brand, in: Ref. [123], 77-89.
- 132 U. Behn and R. Müller, *Phys. Lett.* **113A**, 85 (1985).
- 133 R. Müller and U. Behn, *Z. Phys. B* **69**, 185 (1987).
- 134 R. Müller and U. Behn, *Z. Phys. B* **78**, 229 (1990).
- 135 A. Lange, R. Müller, and U. Behn, *Z. Phys. B* **100**, 477 (1996).
- 136 H. Amm, U. Behn, N. Klöpper, and R. Stannarius, 25. Freiburger Arbeitstagung Flüssigkristalle (1996).
- 137 H. Amm, U. Behn, Th. John, and R. Stannarius, *Mol. Cryst. Liq. Cryst.* **304**, 525 (1997).
- 138 Th. John, Diploma thesis (Universität Leipzig, 1997).
- 139 U. Behn, A. Lange, and Th. John, *Phys. Rev. E* **58**, 2047 (1998).
- 140 U. Behn, Th. John, and R. Stannarius, On-off intermittency in electrohydrodynamic convection in nematics driven by multiplicative noise, in preparation.
- 141 M. Fricke, A. Kühnel, and U. Behn, preprint NTZ 47/1997.
- 142 N. Platt, E. A. Spiegel, and C. Tresser, *Phys. Rev. Lett.* **70**, 279 (1993); J. F. Heagy, N. Platt, and S. M. Hammel, *Phys. Rev.* **49**, 1140 (1994).
- 143 W. Horsthemke and R. Lefever, *Noise induced transitions* (Springer-Verlag, Berlin, 1983).
- 144 R. C. Bourret, U. Frisch, and A. Pouquet, *Physica* **65**, 303 (1973).
- 145 L. Arnold and P. Kloeden, *SIAM J. Appl. Math.* **49**, 1242 (1989).
- 146 L. Arnold and R. Khasminskii, in: *Stochastic Analysis*, Proceedings of Symposia in Pure Mathematics, Volume 57, pp 543, edited by M.C. Cranston and M.A. Pinsky (American Mathematical Society, Providence, Rhode Island, 1995).
- 147 E. Dubois-Violette, *J. Phys. (Paris)* **33**, 95 (1972).
- 148 W. J. A. Goossens, in: *Advances in liquid crystals*, Vol. 3, pp 1, edited by G. H. Brown (Academic Press, New York, 1978).

- 149 The two-dimensional model with free boundary conditions can be adapted to rigid boundary conditions in the one-mode approximation. Since the coefficients look then much less transparent all explicit results were calculated for free boundaries.
- 150 A. Crisanti, G. Paladin, and A. Vulpiani, *Products of Random Matrices in Statistical Physics*, Vol. 104 of *Springer Series in Solid-State Sciences*, edited by M. Cardona, P. Fulde, K. von Klitzing, and H.-J. Queisser (Springer-Verlag, Berlin, 1993).
- 151 V. E. Shapiro and V. M. Loginov, *Physica A* **91**, 563 (1978).
- 152 V. I. Oseledec, *Trans. Moscow Math. Soc.* **19**, 197 (1968).
- 153 N. V. Madhusudana, V. A. Raghunathan, and K. R. Sumathy, *Pramāna, J. Phys.* **28**, L311 (1987).
- 154 J. M. Deutsch, *Phys. Rev. E* **48**, R4179 (1993).
- 155 M. V. Feigel'man and I. E. Staroselsky, *Z. Phys. B* **62**, 261 (1986).
- 156 R. Müller, K. Lippert, A. Kühnel, and U. Behn, *Phys. Rev. E* **56**, 2658 (1997).
- 157 R. Graham, *Phys. Rev. A* **10**, 1762 (1974).
- 158 J. Swift and P. C. Hohenberg, *Phys. Rev. A* **15**, 319 (1977).
- 159 P. C. Hohenberg and J. Swift, *Phys. Rev. A* **46**, 4773 (1992).
- 160 G. De Nigris, G. Nicolis, and H. Frisch, *Phys. Rev. A* **34**, 4211 (1986).
- 161 M. Treiber and L. Kramer, *Phys. Rev. E* **49**, 3184 (1994).
- 162 D.R. Kurtze, *Phys. Rev. Lett.* **77**, 63 (1996).
- 163 J. Viñals, E. Hernández-García, M. San Miguel, and R. Toral, *Phys. Rev. A* **44**, 1123 (1991).
- 164 T. C. Elston and R. F. Fox, *Phys. Rev. A*, **44**, 8403 (1991).
- 165 E. Hernández-García, M. San Miguel, R. Toral, and J. Viñals, *Physica D* **61**, 159 (1992).
- 166 E. Hernández-García, J. Viñals, R. Toral, and M. San Miguel, *Phys. Rev. Lett.* **70**, 3576 (1993).
- 167 J. García-Ojalvo, A. Hernández-Machado, and J. M. Sancho, *Phys. Rev. Lett.* **71**, 1542 (1993).
- 168 L. Ramírez-Piscina, A. Hernández-Machado and J. M. Sancho, *Phys. Rev. B* **48**, 119 (1993).
- 169 L. Ramírez-Piscina, A. Hernández-Machado and J. M. Sancho, *Phys. Rev. B* **48**, 125 (1993).
- 170 J. M. Sancho, A. Hernández-Machado, L. Ramírez-Piscina, and A. M. Lacasta, *Acta Physica Polonica B* **24**, 733 (1993).
- 171 P.-M. Lam and D. Bagayoko, *Phys. Rev. E* **48**, 3267 (1993).
- 172 T. Yamada, *Phys. Lett. A* **161**, 489 (1992).
- 173 T. Yamada, K. Fukushima, and H. Fujisaka, *Physica A* **204**, 755 (1994).
- 174 C. Van den Broeck, J. M. R. Parrondo, J. Armero, and A. Hernández-Machado, *Phys. Rev. E* **49**, 2639 (1994).
- 175 A. Becker and L. Kramer, *Phys. Rev. Lett.* **73**, 955 (1994).
- 176 A. Becker and L. Kramer, *Physica D* **90**, 408 (1996).
- 177 A. Schenzle and H. Brand, *Phys. Rev. A* **20**, 1628 (1979).
- 178 R. Graham and A. Schenzle, *Phys. Rev. A* **25**, 1731 (1982).
- 179 A. Teubel, U. Behn, and A. Kühnel, *Z. Phys. B* **71**, 393 (1988).
- 180 J. Röder, H. Röder, and L. Kramer, *Phys. Rev. E* **55**, 7068 (1997).
- 181 A. Hertrich, W. Pesch, and J. T. Gleeson, *Europhys. Lett.* **44**, 417 (1996).

- 182 J. T. Gleeson, *Nature*, **356**, 511,(1996)
- 183 R. Faller and L. Kramer, *Phys. Rev. E*, **57**, R6249 (1998).
- 184 B. J. Gluckmann, C.B. Arnold and J.P. Gollub *Phys. Rev., E*, **51**, 1128, (1995),  
I. Ning, Y. Hu, R.E. Ecke and G. Ahlers *Phys. Rev. Lett.* **71**, 2216, 1993.
- 185 S. Rudroff and I. Rehberg, *Phys. Rev. E*, **55**, 2742 (1998).
- 186 G. Ahlers, Experiments on thermally driven convection, in A. Buka and L. Kramer, editors, *Pattern formation in liquid crystals*, Springer, (New York 1995).
- 187 L. Thomas, W. Pesch and G. Ahlers, to appear in *Phys.Rev.E*, 1998.
- 188 E. Dubois-Violette and P. Manneville, Flow instabilities in Nematics, in A. Buka and L. Kramer, editors, *Pattern formation in liquid crystals*, Springer, (New York 1995).
- 189 A. P. Krekhov and L. Kramer, *Phys. Rev. E*, **53**, 4925 (1996).
- 190 T. Börzsönyi, A. Buka, A. P. Krekhov and L. Kramer, *Phys. Rev. E*, submitted (1998) (1996).